Spatiotemporally heterogeneous coordination of cholinergic and neocortical activity

Sweyta Lohani[1,5], Andrew H. Moberly[1,5], Hadas Benisty[1], Boris Landa[2], Miao Jing[3], Yulong Li [4], Michael J. Higley [1,6] ✉ & Jessica A. Cardin [1,6] ✉

Variation in an animal's behavioral state is linked to fluctuations in brain activity and cognitive ability. In the neocortex, state-dependent circuit dynamics may reflect neuromodulatory influences such as that of acetylcholine (ACh). Although early literature suggested that ACh exerts broad, homogeneous control over cortical function, recent evidence indicates potential anatomical and functional segregation of cholinergic signaling. In addition, it is unclear whether states as defined by different behavioral markers reflect heterogeneous cholinergic and cortical network activity. Here, we perform simultaneous, dual-color mesoscopic imaging of both ACh and calcium across the neocortex of awake mice to investigate their relationships with behavioral variables. We find that higher arousal, categorized by different motor behaviors, is associated with spatiotemporally dynamic patterns of cholinergic modulation and enhanced large-scale network correlations. Overall, our findings demonstrate that ACh provides a highly dynamic and spatially heterogeneous signal that links fluctuations in behavior to functional reorganization of cortical networks.

Animals cycle through multiple waking brain states that profoundly influence patterns of neuronal activity, perception and behavior[1-4]. Waking states can be categorized by a variety of cognitive and motor variables, including pupil dilation, facial movement, locomotion, arousal and attention[1,5]. However, it is unclear whether variation in these parameters reflects different underlying brain network dynamics. A growing body of research suggests that arousal—measured using a variety of metrics, including elevated motor activity—is associated with distinct alterations in local circuit operations within the neocortex, including changes in mean firing rates and decorrelation of the spike output of neighboring cells[3,6-9]. Moreover, widefield, mesoscopic imaging[10] has revealed broad representation of motor signals across the cortex[8], with changes in behavioral state also linked to reorganization of

functionally connected cortical networks[11,12]. Although desynchronization of local cortical network activity is a hallmark of transitions from periods of quiescence to periods of high arousal or motor output, it is unclear whether large-scale circuits spanning multiple cortical areas also exhibit changes in coordination across state transitions.

Classical views suggest that variation in neural activity associated with behavioral state fluctuations reflects the brain-wide, homogeneous influence of ascending neuromodulatory systems[13]. For example, cholinergic neurons in the basal forebrain send widespread projections throughout the neocortex that are thought to contribute to the effects of arousal, attention and emotional valence on cortical dynamics[5,14-18]. Application of acetylcholine (ACh) evokes desynchronization of local field potentials, decorrelates neuronal spiking and enhances response

[1]Department of Neuroscience, Kavli Institute for Neuroscience, Yale University School of Medicine, New Haven, CT, USA. [2]Program in Applied Mathematics, Yale University, New Haven, CT, USA. [3]Chinese Institute for Brain Research, Beijing, China. [4]State Key Laboratory of Membrane Biology, Peking University School of Life Sciences, PKU-IDG/McGovern Institute for Brain Research, Peking-Tsinghua Center for Life Sciences, Beijing, China. [5]These authors contributed equally: Sweyta Lohani, Andrew H. Moberly. [6]These authors jointly supervised this work: Michael J. Higley, Jessica A. Cardin. ✉e-mail: m.higley@yale.edu; jess.cardin@yale.edu
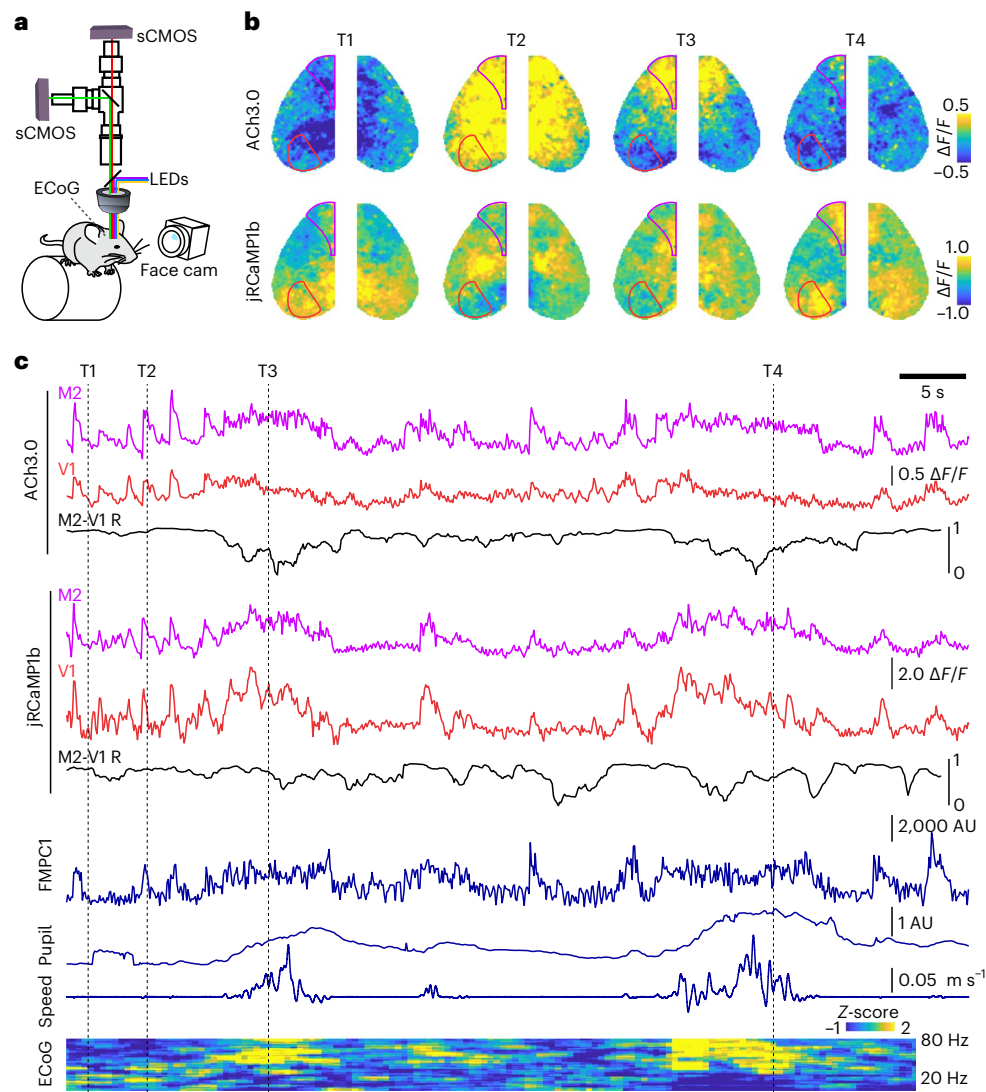
Fig. 1 | Spatiotemporal dynamics of cholinergic and neural activity in the neocortex. a, Schematic of the dual-wavelength, widefield imaging setup. **b**, Example representative image frames showing fluctuations in cholinergic (ACh3.0) and neural (jRCaMP1b) activity across the dorsal cortical surface. Areas marked by red and purple lines indicate Allen Mouse Brain CCFv3-derived parcellation of V1 and M2, respectively. **c**, Time series for ACh3.0 and jRCaMP1b signals in V1 and M2 parcels. Instantaneous (3-s window) Pearson's correlation (*R*) between V1 and M2 is shown beneath in black. Simultaneous facial movement (FaceMap PC1 (FMPC1)), pupil area, running speed and electrocorticogram (ECoG) power spectrogram are shown below. Dashed lines indicate the times of image frames in **b**. AU, arbitrary units.

gain, which are phenomena that are linked to enhanced attention and information representation[6,18–27]. In addition, cholinergic neurons fire strongly to positive and negative reinforcement[28,29], resulting in reinforcement-related plasticity in the cortex[15,30]. These studies suggest that highly salient environmental stimuli may produce uniform ACh signaling across the cortex to enhance global information processing and plasticity. However, recent electrophysiological and anatomical studies indicate substantial diversity in the firing patterns and axonal arborizations of individual cholinergic neurons, suggesting that their output may instead be spatially and temporally heterogeneous in different cortical areas[7,31–34]. Furthermore, the spatiotemporal relationships between cholinergic signaling and cortical neuronal activity across distinct behavioral states are unknown.

To monitor cholinergic activity in vivo has typically required invasive probes with limited spatiotemporal resolution[35]. However, the development of receptor-based fluorescent indicators that directly report ACh binding has opened new avenues for the exploration of neuromodulation. Here, we use dual-color mesoscopic imaging[10] of the red-fluorescent calcium indicator jRCaMP1b[36] and the green-fluorescent ACh indicator ACh3.0 (ref. [37]) across the entire dorsal neocortex of the awake mouse to quantify the relationships between behavioral state, cortical activity and cholinergic signaling. Our results demonstrate that, in contrast to traditional models, different behavioral states (as categorized by motor behavior) are associated with distinct spatiotemporal patterns of ACh fluctuations and increased large-scale network synchronization. Moreover, pharmacological manipulation of muscarinic receptor activity produces spatially distinct alterations in cortical activity. Overall, these findings reshape our view of neuromodulation from a global state variable to a highly dynamic and spatially heterogeneous signal that links fluctuations in behavior to cortical network dynamics.

Results

Dual-color mesoscopic ACh and calcium imaging

To simultaneously monitor neuronal activity and cholinergic signaling in the neocortex of awake mice, we expressed the red-fluorescent

calcium indicator jRCaMP1b[36] and the green-fluorescent ACh sensor ACh3.0 (ref. [37]) throughout the brain via injection of AAV vectors into the transverse sinus of neonatal (postnatal day 0 (P0) and P1) mice[11,38]. This approach resulted in cortex-wide, uniform expression of both reporters (Extended Data Fig. 1), and we confirmed both ex vivo and in vivo that ACh3.0 specifically reported cholinergic signaling (Extended Data Fig. 2). We then performed mesoscopic imaging[10] of both reporters through the intact skull of mice that were head-fixed and freely running on a wheel (Fig. 1a and Methods). Imaging was performed by strobing 575-nm (jRCaMP1b), 470-nm (ACh3.0) and 395-nm (control) excitation light with an overall frame rate of 10 Hz per channel. ACh3.0 and jRCaMP1b images were coregistered, aligned to the Allen Mouse Brain Common Coordinate Framework (CCFv3; Extended Data Fig. 2)[39] and normalized ($\Delta F/F$, where ΔF is the difference from the detrended baseline signal F). There was no observable cross talk between the green (ACh3.0) and red (jRCaMP1b) channels (Extended Data Fig. 2). We removed hemodynamic and motion-related artifacts using a novel regression-based approach that leverages spatial correlations in signal and noise and takes advantage of the reduced ACh-sensitive fluorescence of ACh3.0 when excited at 395 nm (ref. [37]) (Extended Data Fig. 3 and Methods). This method outperformed conventional pixelwise regression in its ability to remove stimulus-induced and spontaneous behavior-associated negative transients in fluorescence corresponding to hemodynamic absorption[40,41] (Extended Data Figs. 3 and 4).

Both ACh and calcium signals exhibited spatially heterogeneous, spontaneous fluctuations across the cortex (Fig. 1b,c), illustrated by example data from two spatially distant cortical areas, the primary visual cortex (V1) and the secondary motor cortex (M2). To investigate the relationship of this activity to behavior, we tracked the animal's state using a combination of variables that are thought to reflect, in different ways, the animal's overall level of arousal (Extended Data Fig. 5 and Supplementary Table 1). Locomotion (wheel running speed) and pupil diameter have been repeatedly linked to variability in behavioral performance[4,42–45] and are associated with distinct patterns of local circuit dynamics[1,3,8,46]. In addition, facial movements like whisking, which reflects the animal's active exploration of its environment, are also closely coupled to cortical function[7,9] and have been captured using FaceMap software to reduce the dimensionality of the facial video data[9]. To complement imaging and behavioral data, we also recorded local circuit dynamics via electrocorticogram (ECoG) in a subset of experiments.

Overall, large fluorescence signal fluctuations occurred across cortical regions for both cholinergic and calcium signals and covaried with changes in pupil dilation, locomotion, facial movement and high-frequency ECoG activity (Fig. 1c). Moreover, interareal correlations for both ACh and calcium were dynamic and tracked variation in behavioral variables[47]. Spatially varied activity patterns in both channels were evident during specific periods of arousal (Fig. 1, highlighted time frames), supporting a model in which ACh release is both dynamic and heterogeneous across cortical regions.

Calcium and cholinergic signals encode behavioral state

To quantify the relationships between behavioral variables and fluorescence activity, we built cross-validated ridge regression models that included facial movements (FaceMap principal component 1 (PC1)–PC25) (Methods), locomotion speed and pupil size as predictors of either ACh or calcium fluctuations for each CCFv3-defined parcel. For ACh3.0 and jRCaMP1b, the variance explained (R^2) using this full model differed significantly across cortical areas (Fig. 2a,b, $P < 0.001$ for ACh3.0 and jRCaMP1b, Friedman's analysis of variance (ANOVA), $n = 6$ mice per group). We also observed significant anterior–posterior gradients in the coupling between behavioral state and fluorescence activity that were inverted for cholinergic versus calcium signals (Fig. 2b, Spearman's rank test), with ACh release and calcium signaling most strongly linked to behavioral state variables in frontal and posterior
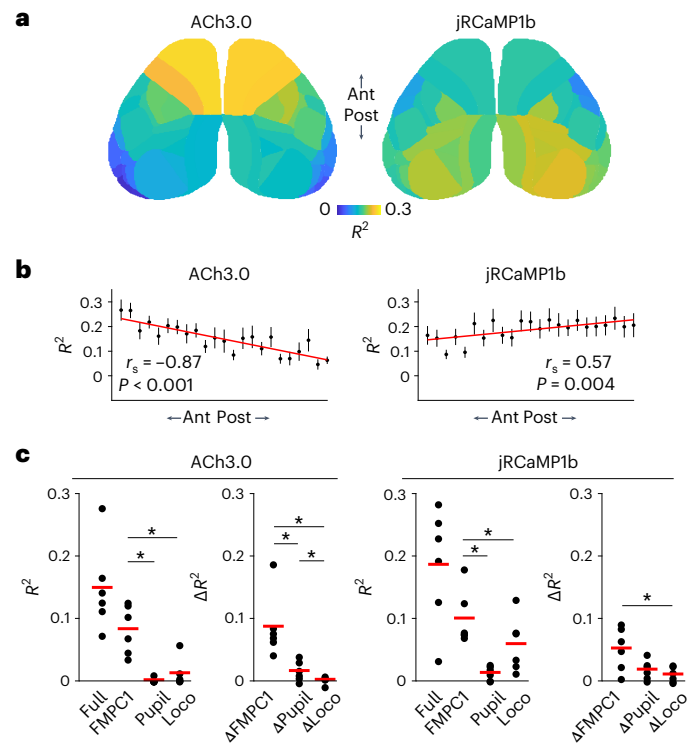

Fig. 2 | Differential coupling of behavioral variables to cholinergic and neural activity across the neocortex. a, Average parcel-wise spatial map ($n = 6$ mice) showing tenfold cross-validated explained variance (R^2) of ACh3.0 and jRCaMP1b signals based on a ridge regression model fitted with FaceMap (PC1–PC25), locomotion and pupil area. **b**, Allen Mouse Brain CCFv3 parcels from one hemisphere were ordered from anterior (Ant) to posterior (Post) based on their center of mass. Cross-validated full-model R^2 values (mean ± s.e.m., $n = 6$ mice) of ACh3.0 and jRCaMP1b are plotted against the parcel's anterior to posterior position. r_s is the Spearman's rank-order correlation coefficient for the correlation between mean R^2 and anterior–posterior rank across parcels (ACh3.0 $r_s = -0.871$, $P < 0.0001$; jRCaMP1b $r_s = 0.574$, $P = 0.004$). Red line indicates linear fit for visualization purposes. **c**, For each signal, left panels show the cross-validated R^2 (averaged across parcels in one hemisphere) for the full model (Full) and for single-variable models (FaceMap PC1 (FMPC1), pupil area (Pupil) and locomotion (Loco)). Right panels show the unique contribution of each variable (ΔR^2). *$P < 0.05$ for post hoc two-tailed Wilcoxon signed-rank tests (for ACh3.0 R^2, $P = 0.031$ for FaceMap vs pupil, $P = 0.031$ for FaceMap vs locomotion and $P = 0.063$ for pupil vs locomotion; for ACh3.0 ΔR^2, $P = 0.031$ for FaceMap vs pupil, $P = 0.031$ for FaceMap vs locomotion and $P = 0.031$ for pupil vs locomotion; for jRCaMP1b R^2, $P = 0.031$ for FaceMap vs pupil, $P = 0.031$ for FaceMap vs locomotion and $P = 0.063$ for pupil vs locomotion; and for jRCaMP1b ΔR^2, $P = 0.063$ for FaceMap vs pupil, $P = 0.031$ for FaceMap vs locomotion and $P = 0.438$ for pupil vs locomotion) following a significant Friedman's ANOVA (for ACh3.0 R^2, $\chi^2(2) = 10.333$, $P = 0.006$; for ACh3.0 ΔR^2, $\chi^2(2) = 12.000$, $P = 0.003$; for jRCaMP1b R^2, $\chi^2(2) = 10.333$, $P = 0.006$; and for jRCaMP1b ΔR^2, $\chi^2(2) = 7.000$, $P = 0.030$; $n = 6$ mice).

areas, respectively. To examine the relative relationships between each behavioral metric and neural activity, we first constructed a full model while temporally shuffling the data for one predictor and calculating the change in predictive power (ΔR^2), reflecting the unique contribution of the shuffled variable. We also constructed single-predictor models to examine the ability of each variable to predict neural activity[8] (Methods). For facial movements, we explicitly examined the contribution of FaceMap PC1. For ACh3.0, both single-variable and shuffled models produced similar results with significant differences between behavioral metrics (Fig. 2c). Facial movements (FaceMap PC1) yielded the
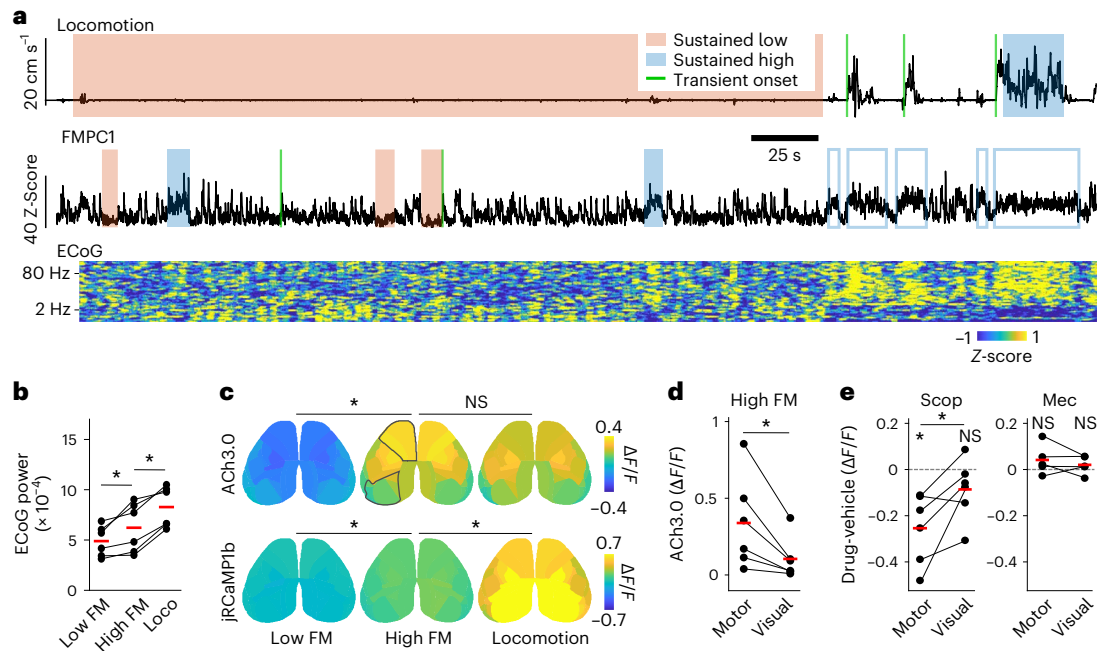
Fig. 3 | Cholinergic and neural signal heterogeneity during movement-defined behavioral states. a, Example locomotion and FaceMap PC1 traces from an experimental session. Periods of sustained low or high motor activity are indicated by shaded regions and transitions from low to high motor activity are delineated by green lines. Open blue boxes indicate high facial movement (FM) periods not included in analysis of sustained facial motor activity periods due to overlap with locomotion. **b**, Individual animal values (n = 6 mice) and population means for high-frequency (30–100 Hz) ECoG power for sustained low facial movement, high facial movement and locomotion states. *P < 0.05 for post hoc two-tailed paired t-test comparisons ($t(5)$ = −2.600, P = 0.048 for low FM vs high FM; $t(5)$ = −6.165, P = 0.002 for locomotion vs high FM) following a significant (P < 0.05) main effect of behavioral state in repeated measures ANOVA ($F_{2,10}$ = 38.794, P < 0.001). **c**, Average spatial maps (n = 6 mice) showing ACh3.0 and jRCaMP1b $\Delta F/F$ activity during three movement-defined sustained behavioral states. *P < 0.05 for post hoc two-tailed paired t-test comparisons (for ACh3.0, $t(5)$ = −2.646, P = 0.046 for low vs high FM and $t(5)$ = 0.384, P = 0.717

for locomotion vs high FM; and for jRCaMP1b, $t(5)$ = −3.367, P = 0.020 for low vs high FM and $t(5)$ = −2.672, P = 0.044 for locomotion vs high FM) following a significant (P < 0.05) main effect of behavioral state in repeated measures ANOVA (for ACh3.0, $F_{2,10}$ = 6.528, P = 0.015; and for jRCaMP1b, $F_{2,10}$ = 9.251, P = 0.005). **d**, ACh3.0 amplitude (n = 6 mice) in frontal-motor areas compared to visual areas during high facial movement ($t(5)$ = −3.210, P = 0.024, two-tailed paired t-test). **e**, Change in jRCaMP1b signal in frontal-motor and visual areas during treatment with scopolamine (Scop; 0.5 mg kg^{-1} i.p., n = 6 mice) and mecamylamine (Mec; 1 mg kg^{-1} i.p., n = 5 mice). The effect of each drug is shown as $\Delta F/F$ difference between drug and vehicle sessions within animal. *P < 0.05 for one-sample two-tailed t-test within each brain region ($t(5)$ = −4.104, P = 0.009 for scopolamine motor; $t(5)$ = −1.599, P = 0.171 for scopolamine visual; $t(4)$ = 1.444, P = 0.222 for mecamylamine motor; and $t(4)$ = 1.169, P = 0.307 for mecamylamine visual) and two-tailed paired t-test between brain regions ($t(5)$ = −2.856, P = 0.036 for scopolamine; and $t(4)$ = 0.907, P = 0.416 for mecamylamine). NS, not significant.

strongest prediction accuracy compared with locomotion and pupil variation for ACh3.0 (Fig. 2c, Extended Data Fig. 6). For jRCaMP1b, both single-predictor R^2 and ΔR^2 measures differed significantly by state (Fig. 2c). Again, facial movement was the most robust predictor (Fig. 2c, Extended Data Fig. 6). For both ACh3.0 and jRCamp1b, FaceMap principal components explained most of the variance in the data, with the first component alone outperforming other behavioral metrics (Extended Data Fig. 6). These results indicate that cholinergic release, like intracortical dynamics[8,9], encodes some forms of motor behavior and that distinct behavioral states are differentially coupled to neural activity. Statistical results for these and all subsequent analyses are listed in Supplementary Tables 2 and 3.

State-dependent variation in brain activity might be accompanied by either transient or sustained changes in cholinergic and calcium signals that reflect underlying circuit dynamics. Therefore, we focused on discrete epochs of motor activity and identified time points corresponding to the onset of either locomotion or facial movements (Fig. 3a and Methods). Facial movement onset (quantified using FaceMap PC1) in the absence of locomotion was associated with desynchronization of local neuronal firing as estimated by ECoG[45] and significant whole-cortex-averaged transients in both ACh signals (0.64 ± 0.09 $\Delta F/F$, P = 0.001, Student's t-test, n = 6 mice) and calcium signals (0.69 ± 0.15 $\Delta F/F$, P = 0.006, Student's t-test, n = 6 mice) (Extended Data Fig. 7).

Locomotion onset was associated with an increase in facial movement and local desynchronization and with transient increases in ACh signals (0.68 ± 0.17 $\Delta F/F$, P = 0.010, Student's t-test, n = 6 mice) and calcium signals (1.50 ± 0.11 $\Delta F/F$, P < 0.001, Student's t-test, n = 6 mice) (Extended Data Fig. 7). ACh transients varied significantly across cortical areas (P < 0.001) but were not significantly different between locomotion and facial movement onsets (P = 0.734, two-way repeated measures ANOVA, n = 6 mice per group). Calcium transients varied significantly across cortical areas (P < 0.001) and states (P = 0.005, two-way repeated measures ANOVA, n = 6 mice per group), with locomotion onset associated with the largest signal (Extended Data Fig. 7). We also found a significant anterior–posterior gradient in the transient magnitudes for cholinergic but not calcium signals (Extended Data Fig. 7).

Next, we analyzed periods of sustained low or high motor activity (Fig. 3a and Methods). We observed that quiescence included epochs of both low and high facial movement, whereas locomotion always co-occurred with high facial movement, suggesting that arousal might follow a progression from absence of motor activity to facial movement and then to locomotion. Sustained increases in facial movement and locomotion were associated with progressively increasing local circuit desynchronization, as evidenced by an increase in high-frequency power (Fig. 3b) and a corresponding decrease in low-frequency power (Extended Data Fig. 7e) in the ECoG. We then examined the relationship
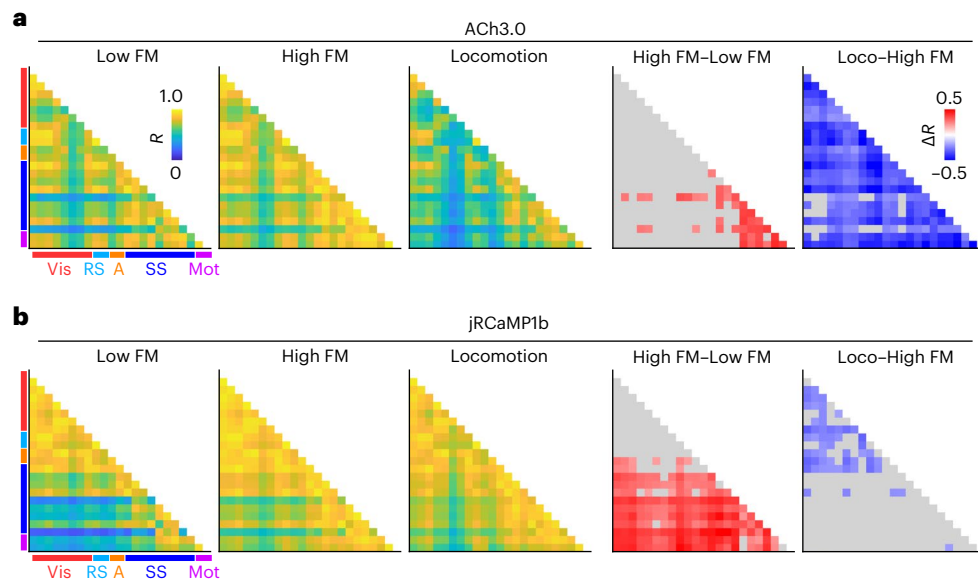
Fig. 4 | State-dependent variation in spatial correlations of cholinergic and neural activity. a, Average peak cross-correlation matrices ($n = 6$ mice) for cholinergic activity during three movement-defined behavioral states (namely, low facial movement, high facial movement and locomotion) measured pairwise for CCFv3-defined cortical parcels in the left hemisphere (first, second and third columns). Average differences in correlation between high and low facial movement states (fourth column) and between locomotion and high facial movement states (fifth column) are shown for significant pairs (adjusted $P < 0.01$, Benjamini–Yekutieli FDR-corrected two-tailed permutation test, $n = 6$ mice) (Supplementary Table 3). Nonsignificant pairs are shown in gray. A, Auditory; Mot, Motor; RS, retrosplenial; SS, somatosensory; Vis, Visual. **b**, As in **a** but for calcium (jRCaMP1b) activity.

of these three sustained states with cholinergic and calcium activity across cortical areas. ACh activity varied significantly across cortical areas ($P < 0.001$) and differed by state ($P = 0.015$, two-way repeated measures ANOVA, $n = 6$ mice per group). Sustained facial movement significantly elevated whole-cortex ACh activity (low facial movement, $-0.13 \pm 0.04 \, \Delta F/F$; high facial movement, $0.18 \pm 0.08 \, \Delta F/F$) but locomotion did not further increase the ACh signal (locomotion, $0.16 \pm 0.06 \, \Delta F/F$) (Fig. 3c). Similarly, sustained calcium activity varied significantly for cortical area ($P < 0.001$) and state ($P = 0.005$, two-way repeated measures ANOVA, $n = 6$ mice per group). Sustained facial movement and locomotion both increased whole-cortex calcium activity (low facial movement, $-0.02 \pm 0.02 \, \Delta F/F$; high facial movement, $0.17 \pm 0.04 \, \Delta F/F$; locomotion, $0.63 \pm 0.19 \, \Delta F/F$; low versus high facial movement, $P = 0.020$) (Fig. 3c). As with transients, there was a significant anterior–posterior gradient in the differences across states, measured with Spearman's rank-order correlation (comparing sustained high and low facial movement for the cholinergic signal and comparing sustained locomotion and high facial movement for calcium activity) (Extended Data Fig. 7). We also confirmed that these results were not unique to imaging ACh release directly, as we observed a similar relationship between behavioral state and cholinergic axonal signaling, as measured by mesoscopic imaging of genetically targeted GCaMP6s-expressing fibers (Extended Data Fig. 8).

Our results indicate that increased motor activity (for example, facial movement) is associated with significantly higher ACh release in motor versus visual areas (Fig. 3d). To experimentally test whether this spatial heterogeneity corresponds to differential modulation of neural circuits, we examined the consequences of pharmacologically manipulating cholinergic receptors (Methods). Consistent with ACh3.0 imaging, treatment with the muscarinic blocker scopolamine selectively decreased cortical activity in motor but not visual areas (Fig. 3e). By contrast, treatment with the nicotinic blocker mecamylamine had no significant effect on cortical activity (Fig. 3e). Together, these results suggest a spatially heterogeneous and state-dependent relationship between cortical ACh release and cortical activity.

State-dependent modulation of cortical network architecture

Behavior is thought to rely on large-scale coordination of activity between cortical areas[47–49]. Therefore, we next examined the spatiotemporal relationships of both ACh and calcium signals by measuring pairwise correlations between cortical regions. We focused on sustained periods of low facial movement, high facial movement and locomotion, allowing us to test whether these behavioral states with different average increases in fluorescence signals also correspond to distinct changes in network organization. We found that increased facial movement was associated with significant increases in between-area pairwise correlations in anterior somatosensory and motor areas for ACh signal and broad, significant increases for calcium signal (Fig. 4a,b and Extended Data Fig. 9). In marked contrast, locomotion was associated with a reduction in the between-area correlations of cholinergic activity that was significant across the cortex (Fig. 4a). Locomotion was also associated with modest decreases in correlation of calcium signals that were significant primarily across posterior cortical areas (Fig. 4b). We note that the limited number of pixels present for the most lateral CCFv3 parcels probably decreases the robustness of correlation measurements for these areas. Overall, our results suggest that moderate levels of arousal (that is, facial movement without locomotion) generally enhance the coordination of ACh release in the cortex, but high levels of arousal (that is, locomotion) profoundly decorrelate cholinergic signals, emphasizing the spatiotemporal independence of cholinergic modulation. Moreover, in contrast to the local network decorrelation associated with enhanced arousal (observed in the ECoG data), we find that facial movement is linked to significantly increased correlation across large-scale networks, as measured by calcium imaging.

Increases in cholinergic signaling have been linked to enhanced local neuronal firing and response gain[6,18,24,50,51]. We therefore investigated whether ACh and calcium signals are coupled to each other within individual cortical areas and whether this relationship varies with behavioral state. Sustained facial movement was associated with a significant increase in correlation between the two signals broadly across the cortex (Fig. 5a,b and Extended Data Fig. 9). In striking contrast,
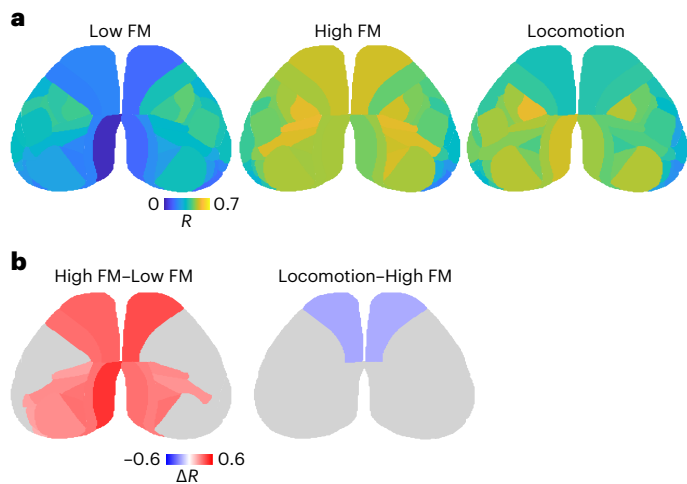
Fig. 5 | State-dependent spatial variation in correlations between cholinergic and calcium signals. a, Average spatial maps (*n* = 6 mice) showing peak cross-correlation coefficients between ACh3.0 and jRCaMP1b activity for each cortical parcel during three movement-defined behavioral states: low facial movement, high facial movement and locomotion. **b**, Average difference in correlation between high and low facial movement states and between locomotion and high facial movement states is shown for significant parcels (adjusted *P* < 0.01, Benjamini–Yekutieli FDR-corrected two-tailed permutation test, *n* = 6 mice) (Supplementary Table 3). Nonsignificant parcels are shown in gray.

Fig. 6 | Relationship between arousal, cortical activity and network synchrony. Arousal is associated with distinct patterns of motor activity, marked by elevated facial movement energy arising from movements of whiskers and facial muscles and by locomotion, which always co-occurs with facial movement. Higher arousal corresponds to elevated neuronal activity and ACh release across the neocortex. As arousal increases, correlations within local cortical circuits measured via ECoG progressively decrease. By contrast, correlations within large-scale networks and in ACh release across the cortex, as measured by mesoscopic imaging, increase during moderate arousal associated with high facial movement but decrease with higher arousal that is associated with locomotion.

sustained locomotion was associated with a significant reduction in the correlation between the two channels that was restricted to the frontal cortex (Fig. 5a,b, Extended Data Fig. 9). These data suggest that cholinergic coupling to neuronal activity varies with both cortical area and behavioral state. Overall, our findings demonstrate a spatially compartmentalized relationship between cholinergic modulation and cortical activity that is diversely dependent on transitions between distinct behavioral states.

Discussion

Despite a long history of investigation into the role of cholinergic modulation in the neocortex, experimental challenges to large-scale simultaneous monitoring of ACh release and neural activity in vivo have limited our understanding. Indeed, consistent observations that ACh is coupled to salient behavioral cues across sensory modalities might suggest that this modulatory pathway serves as a global, homogeneous influence throughout the cortex[13,52]. Here, we challenged this view using a combination of mesoscopic imaging and newly developed reporters of both calcium and ACh in behaving mice. Our results clearly demonstrate that cholinergic signaling exhibits substantial spatiotemporal fluctuations that are differentially related to distinct behavioral states, defined by patterns of motor activity.

Both facial movements and locomotion are associated with significant, broad increases in ACh release that are enhanced for anterior versus posterior areas. This anterior–posterior gradient could map onto slightly differential cholinergic projection densities in the frontal versus parietal and occipital areas, to rough anteroposterior and mediolateral projection topography from the basal forebrain and/or to different ratios of basal forebrain cholinergic to noncholinergic (GABAergic) projections for frontal and posterior cortical areas[31,53,54]. Interestingly, we find that facial movement is coupled to significantly synchronized ACh release across the anterior cortex. By contrast, locomotion, which co-occurs with facial movement, is coupled to robust, cortex-wide desynchronization of cholinergic activity. This result emphasizes the fundamental independence of cholinergic signaling across different cortical areas and is consistent with anatomical and
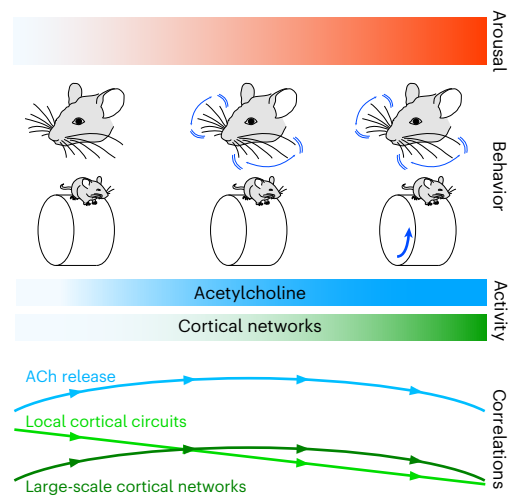
electrophysiological heterogeneity within populations of cholinergic projection neurons in the basal forebrain[31,33,34,55,56]. We speculate that information about behavioral states is relayed broadly to the entire basal forebrain, which then propagates independently via discrete channels to selective areas of the cortex. Such a system would allow independent, behavior-specific modulation of cortical subnetworks. We also note that ACh can be released locally by subpopulations of cortical interneurons, providing an additional mechanism for heterogeneous cholinergic modulation[57].

Motor behavior is closely linked to fluctuations in the activity of neurons across the neocortex, suggesting that the representation of movement is a fundamental feature of cortical networks[8,9,58]. Here, we find similarly that facial movements and locomotion are represented in ACh signals. Regression analyses suggest that facial motor information is most prominent, contrasting with recent observations showing that cholinergic axonal activity is strongly coupled to pupil dynamics[46]. We note that, unlike axonal calcium imaging, ACh3.0 reports cholinergic release, and the transfer function between presynaptic calcium and transmitter exocytosis in vivo is poorly characterized[59]. In this way, our approach is similar to electrochemical measurement of cholinergic release[60] but capable of stable, longitudinal monitoring across the entire dorsal cortex in the absence of invasive probes. Nevertheless, we found similar spatial patterns of cholinergic signaling when imaging ACh release (via ACh3.0) or presynaptic axonal activity (via GCaMP6s), suggesting that our results are not specific to signal modality. Importantly, none of these methods provide information regarding the physiological extent of ACh reception or cell type-specific downstream signaling, which ultimately requires tools for monitoring both postsynaptic biochemical activity and spike output at cellular resolution[61].

In the neocortex, both motor activity and cholinergic signaling have been linked to the desynchronization of local circuits and the decorrelation of spiking between neighboring neurons[6,21,22,24,62]. Such electrophysiological changes are suggested to enhance the representation of information, particularly under demanding cognitive regimes such as focused attention[63]. However, the coordination of sensory, motor and

cognitive networks is also thought to be necessary for behavior[1,8,9,64]. Here, we find the surprising result that increases in motor activity and ACh release are associated with significant increases in long-range, intracortical correlations even though local circuits are decorrelated.

Recognition of behavioral state as a critical determinant of cortical function and behavior has increased only in recent years, but the diversity of studies has left a number of ambiguities unresolved. For example, variations in arousal, attention, locomotion, whisking, facial movements and pupil diameter have all been linked to cortical dynamics and modulation of perceptual ability[1–4,44]. The extent to which these categorizations reflect distinct or overlapping mechanisms and computations remains largely unknown. Indeed, previous work found that arousal without locomotion and arousal accompanied by locomotion exert distinct influences on local cortical activity patterns, but both enhance sensory encoding[3]. Nevertheless, our findings here support the hypothesis that waking comprises diverse behavioral states characterized by specific patterns of neuromodulatory dynamics[3,13]. Indeed, our data suggest that arousal and neuromodulation may follow a progression that parallels motor activity, first manifesting with facial movement and increasing with locomotion (Fig. 6). In this model, moderate arousal drives an increase in ACh release and cortical activity that is coupled to a decorrelation of local circuits and enhanced large-scale synchrony. Further arousal associated with locomotion drives desynchronized ACh release, local circuit decorrelation and global correlation of broad intracortical networks. The causal links between these dynamics remain to be determined. However, the continued development of multicolor fluorescent reporters, novel combinations of imaging modalities and electrophysiology[11,12,37,65] and further refinement of behavioral analyses[9,66] may present new avenues to resolve these issues.

In conclusion, we provide evidence for the idea that movement is broadly represented in the cortex, not only in local circuit activity[8,9] but also in the dynamics of cholinergic modulation. Furthermore, cholinergic output during movement is spatially structured and nonuniform in the cortex. Additional studies are required to determine whether these common patterns reflect movement-related ascending regulation of cortical networks or top-down, state-dependent control of basal forebrain output[13]. In either case, we propose the broad hypothesis that the fine-tuned orchestration of behavioral and cortical state dynamics requires coordinated coupling of neuronal activity and cholinergic modulation within distinct, spatially heterogeneous networks of the neocortex.

Online content

Any methods, additional references, Nature Portfolio reporting summaries, source data, extended data, supplementary information, acknowledgements, peer review information; details of author contributions and competing interests; and statements of data and code availability are available at https://doi.org/10.1038/s41593-022-01202-6.

References

1. McGinley, M. J. et al. Waking state: rapid variations modulate neural and behavioral responses. *Neuron* **87**, 1143–1161 (2015).
2. Niell, C. M. & Stryker, M. P. Modulation of visual responses by behavioral state in mouse visual cortex. *Neuron* **65**, 472–479 (2010).
3. Vinck, M., Batista-Brito, R., Knoblich, U. & Cardin, J. A. Arousal and locomotion make distinct contributions to cortical activity patterns and visual encoding. *Neuron* **86**, 740–754 (2015).
4. Tang, L. & Higley, M. J. Layer 5 circuits in V1 differentially control visuomotor behavior. *Neuron* **105**, 346–354.e5 (2020).
5. Poulet, J. F. A. & Crochet, S. The cortical states of wakefulness. *Front. Syst. Neurosci.* **12**, 64 (2018).
6. Chen, N., Sugihara, H. & Sur, M. An acetylcholine-activated microcircuit drives temporal dynamics of cortical activity. *Nat. Neurosci.* **18**, 892–902 (2015).
7. Munoz, W. & Rudy, B. Spatiotemporal specificity in cholinergic control of neocortical function. *Curr. Opin. Neurobiol.* **26**, 149–160 (2014).
8. Musall, S., Kaufman, M. T., Juavinett, A. L., Gluf, S. & Churchland, A. K. Single-trial neural dynamics are dominated by richly varied movements. *Nat. Neurosci.* **22**, 1677–1686 (2019).
9. Stringer, C. et al. Spontaneous behaviors drive multidimensional, brainwide activity. *Science* **364**, 255 (2019).
10. Cardin, J. A., Crair, M. C. & Higley, M. J. Mesoscopic imaging: shining a wide light on large-scale neural dynamics. *Neuron* **108**, 33–43 (2020).
11. Barson, D. et al. Simultaneous mesoscopic and two-photon imaging of neuronal activity in cortical circuits. *Nat. Methods* **17**, 107–113 (2020).
12. Clancy, K. B., Orsolic, I. & Mrsic-Flogel, T. D. Locomotion-dependent remapping of distributed cortical networks. *Nat. Neurosci.* **22**, 778–786 (2019).
13. Lee, S. H. & Dan, Y. Neuromodulation of brain states. *Neuron* **76**, 209–222 (2012).
14. Buzsaki, G. et al. Nucleus basalis and thalamic control of neocortical activity in the freely moving rat. *J. Neurosci.* **8**, 4007–4026 (1988).
15. Chubykin, A. A., Roach, E. B., Bear, M. F. & Shuler, M. G. A cholinergic mechanism for reward timing within primary visual cortex. *Neuron* **77**, 723–735 (2013).
16. Picciotto, M. R., Higley, M. J. & Mineur, Y. S. Acetylcholine as a neuromodulator: cholinergic signaling shapes nervous system function and behavior. *Neuron* **76**, 116–129 (2012).
17. Goard, M. & Dan, Y. Basal forebrain activation enhances cortical coding of natural scenes. *Nat. Neurosci.* **12**, 1444–1449 (2009).
18. Herrero, J. L. et al. Acetylcholine contributes through muscarinic receptors to attentional modulation in V1. *Nature* **454**, 1110–1114 (2008).
19. Constantinople, C. M. & Bruno, R. M. Effects and mechanisms of wakefulness on local cortical networks. *Neuron* **69**, 1061–1068 (2011).
20. Eggermann, E., Kremer, Y., Crochet, S. & Petersen, C. C. H. Cholinergic signals in mouse barrel cortex during active whisker sensing. *Cell Rep.* **9**, 1654–1660 (2014).
21. Meir, I., Katz, Y. & Lampl, I. Membrane potential correlates of network decorrelation and improved SNR by cholinergic activation in the somatosensory cortex. *J. Neurosci.* **38**, 10692–10708 (2018).
22. Metherate, R., Cox, C. L. & Ashe, J. H. Cellular bases of neocortical activation: modulation of neural oscillations by the nucleus basalis and endogenous acetylcholine. *J. Neurosci.* **12**, 4701–4711 (1992).
23. Minces, V., Pinto, L., Dan, Y. & Chiba, A. A. Cholinergic shaping of neural correlations. *Proc. Natl Acad. Sci. USA* **114**, 5725–5730 (2017).
24. Pinto, L. et al. Fast modulation of visual perception by basal forebrain cholinergic neurons. *Nat. Neurosci.* **16**, 1857–1863 (2013).
25. Steriade, M., Contreras, D., Curro Dossi, R. & Nunez, A. The slow (< 1 Hz) oscillation in reticular thalamic and thalamocortical neurons: scenario of sleep rhythm generation in interacting thalamic and neocortical networks. *J. Neurosci.* **13**, 3284–3299 (1993).
26. Steriade, M., Nunez, A. & Amzica, F. Intracellular analysis of relations between the slow (< 1 Hz) neocortical oscillation and other sleep rhythms of the electroencephalogram. *J. Neurosci.* **13**, 3266–3283 (1993).
27. Gasselin, C., Hohl, B., Vernet, A., Crochet, S. & Petersen, C.C.H. Cell-type-specific nicotinic input disinhibits mouse barrel cortex during active sensing. *Neuron* **109**, 778–787.e3 (2021).

28. Hangya, B., Ranade, S. P., Lorenc, M. & Kepecs, A. Central cholinergic neurons are rapidly recruited by reinforcement feedback. *Cell* **162**, 1155–1168 (2015).

29. Sturgill, J. F. et al. Basal forebrain-derived acetylcholine encodes valence-free reinforcement. Preprint at *bioRxiv* https://doi.org/10.1101/2020.02.17.953141 (2020).

30. Guo, W., Robert, B. & Polley, D. B. The cholinergic basal forebrain links auditory stimuli with delayed reinforcement to support learning. *Neuron* **103**, 1164–1177.e6 (2019).

31. Kim, J. H. et al. Selectivity of neuromodulatory projections from the basal forebrain and locus ceruleus to primary sensory cortices. *J. Neurosci.* **36**, 5314–5327 (2016).

32. Laszlovszky, T. et al. Distinct synchronization, cortical coupling and behavioral function of two basal forebrain cholinergic neuron types. *Nat. Neurosci.* **23**, 992–1003 (2020).

33. Li, X. et al. Generation of a whole-brain atlas for the cholinergic system and mesoscopic projectome analysis of basal forebrain cholinergic neurons. *Proc. Natl Acad. Sci. USA* **115**, 415–420 (2018).

34. Zaborszky, L. et al. Neurons in the basal forebrain project to the cortex in a complex topographic organization that reflects corticocortical connectivity patterns: an experimental study based on retrograde tracing and 3D reconstruction. *Cereb. Cortex* **25**, 118–137 (2015).

35. Disney, A. A. & Higley, M. J. Diverse spatiotemporal scales of cholinergic signaling in the neocortex. *J. Neurosci.* **40**, 720–725 (2020).

36. Dana, H. et al. Sensitive red protein calcium indicators for imaging neural activity. *eLife* **5**, e12727 (2016).

37. Jing, M. et al. An optimized acetylcholine sensor for monitoring in vivo cholinergic activity. *Nat. Methods* **17**, 1139–1146 (2020).

38. Hamodi, A. S., Martinez Sabino, A., Fitzgerald, N. D., Moschou, D. & Crair, M. C. Transverse sinus injections drive robust whole-brain expression of transgenes. *eLife* **9**, e53639 (2020).

39. Wang, Q. et al. The Allen Mouse Brain Common Coordinate Framework: a 3D reference atlas. *Cell* **181**, 936–953 e920 (2020).

40. Ma, Y. et al. Wide-field optical mapping of neural activity and brain haemodynamics: considerations and novel approaches. *Phil. Trans. R. Soc. Lond. B* **371**, 20150360 (2016).

41. Valley, M. T. et al. Separation of hemodynamic signals from GCaMP fluorescence measured with wide-field imaging. *J. Neurophysiol.* **123**, 356–366 (2020).

42. Bennett, C., Arroyo, S. & Hestrin, S. Subthreshold mechanisms underlying state-dependent modulation of visual responses. *Neuron* **80**, 350–357 (2013).

43. McGinley, M. J., David, S. V. & McCormick, D. A. Cortical membrane potential signature of optimal states for sensory signal detection. *Neuron* **87**, 179–192 (2015).

44. Neske, G. T., Nestvogel, D., Steffan, P. J. & McCormick, D. A. Distinct waking states for strong evoked responses in primary visual cortex and optimal visual detection performance. *J. Neurosci.* **39**, 10044–10059 (2019).

45. Perrenoud, Q. et al. Flexible perceptual encoding by discrete gamma events. Preprint at *bioRxiv* https://doi.org/10.1101/2022.1105.1113.491832 (2022).

46. Reimer, J. et al. Pupil fluctuations track rapid changes in adrenergic and cholinergic activity in cortex. *Nat. Commun.* **7**, 13289 (2016).

47. Benisty, H. et al. Rapid fluctuations in functional connectivity of cortical networks encode spontaneous behavior. Preprint at *bioRxiv* https://doi.org/10.1101/2021.1108.1115.456390 (2021).

48. Rubinov, M. & Sporns, O. Complex network measures of brain connectivity: uses and interpretations. *Neuroimage* **52**, 1059–1069 (2010).

49. Stafford, J. M. et al. Large-scale topology and the default mode network in the mouse connectome. *Proc. Natl Acad. Sci. USA* **111**, 18745–18750 (2014).

50. Parikh, V., Kozak, R., Martinez, V. & Sarter, M. Prefrontal acetylcholine release controls cue detection on multiple timescales. *Neuron* **56**, 141–154 (2007).

51. Soma, S., Shimegi, S., Suematsu, N. & Sato, H. Cholinergic modulation of response gain in the rat primary visual cortex. *Sci Rep.* **3**, 1138 (2013).

52. Hasselmo, M. E. & Sarter, M. Modes and models of forebrain cholinergic neuromodulation of cognition. *Neuropsychopharmacology* **36**, 52–73 (2011).

53. Avendano, C., Umbriaco, D., Dykes, R. W. & Descarries, L. Acetylcholine innervation of sensory and motor neocortical areas in adult cat: a choline acetyltransferase immunohistochemical study. *J. Chem. Neuroanat.* **11**, 113–130 (1996).

54. Bigl, V., Woolf, N. J. & Butcher, L. L. Cholinergic projections from the basal forebrain to frontal, parietal, temporal, occipital, and cingulate cortices: a combined fluorescent tracer and acetylcholinesterase analysis. *Brain Res. Bull.* **8**, 727–749 (1982).

55. Chaves-Coira, I., Barros-Zulaica, N., Rodrigo-Angulo, M. & Nunez, A. Modulation of specific sensory cortical areas by segregated basal forebrain cholinergic neurons demonstrated by neuronal tracing and optogenetic stimulation in mice. *Front. Neural Circuits* **10**, 28 (2016).

56. Gielow, M. R. & Zaborszky, L. The input-output relationship of the cholinergic basal forebrain. *Cell Rep.* **18**, 1817–1830 (2017).

57. Granger, A. J. et al. Cortical ChAT⁺ neurons co-transmit acetylcholine and GABA in a target- and brain-region-specific manner. *eLife* **9**, e57749 (2020).

58. Parker, P. R. L., Brown, M. A., Smear, M. C. & Niell, C. M. Movement-related signals in sensory areas: roles in natural behavior. *Trends Neurosci.* **43**, 581–595 (2020).

59. Sudhof, T. C. Calcium control of neurotransmitter release. *Cold Spring Harb. Perspect. Biol.* **4**, a011353 (2012).

60. Sarter, M. & Kim, Y. Interpreting chemical neurotransmission in vivo: techniques, time scales, and theories. *ACS Chem. Neurosci.* **6**, 8–10 (2015).

61. Lee, S. J. et al. Cell-type-specific asynchronous modulation of PKA by dopamine in learning. *Nature* **590**, 451–456 (2020).

62. Polack, P. O., Friedman, J. & Golshani, P. Cellular mechanisms of brain state-dependent gain modulation in visual cortex. *Nat. Neurosci.* **16**, 1331–1339 (2013).

63. Thiele, A. & Bellgrove, M. A. Neuromodulation of attention. *Neuron* **97**, 769–785 (2018).

64. Crochet, S., Lee, S. H. & Petersen, C. C. H. Neural circuits for goal-directed sensorimotor transformations. *Trends Neurosci.* **42**, 66–77 (2019).

65. Esmaeili, V. et al. Rapid suppression and sustained activation of distinct cortical regions for a delayed sensory-triggered motor response. *Neuron* **13**, 2183–2201 (2021).

66. Mathis, A. et al. DeepLabCut: markerless pose estimation of user-defined body parts with deep learning. *Nat. Neurosci.* **21**, 1281 (2018).

Methods

Animals

Male and female C57BL/6J, ChAT-Cre (B6J.ChAT-IRES-Cre::frt-neo-frt, JAX stock no. 028861), Slc17a7-cre/Camk2α-tTA/TITL-GCaMP6f (JAX stock nos. 023527 and 024108) and Thy1-GCamp6f (JAX stock no. 024276) mice (2–6 months) were kept on a 12-h light/dark cycle, provided with food and water ad libitum and housed individually following headpost implantations. Imaging experiments were performed during the light phase of the cycle. All animal handling and experiments were performed according to the ethical guidelines of the Institutional Animal Care and Use Committee of the Yale University School of Medicine.

Neonatal sinus injections

Brain-wide expression of the ACh sensor ACh3.0 and the calcium indicator jRCaMP1b was achieved by postnatal sinus injection[11,38]. Specifically, P0–P1 litters were removed from their home cage and placed on a heating pad. Pups were kept on ice for 5 min to induce anesthesia via hypothermia and then maintained on a metal plate surrounded by ice for the duration of the injection. Under a dissecting microscope, two small incisions were made in the skin over the transverse sinuses. Viral injections were made with a NanoFil (WPI) attached to a 36-gauge needle and an UltraMicroPump (WPI) mounted to a stereotaxic arm. The needle was slowly lowered through the skull into the underlying transverse sinus. Pups were injected bilaterally with 2 μl of AAV9-hsyn-ACh3.0 (1.8×10^{13} gc ml^{-1}) and 2 μl of AAV9-hsyn-NES-jRCaMP1b (2.5×10^{13} gc ml^{-1}; Addgene) per hemisphere. The hsyn promoter drives expression in most excitatory neurons. A subset of pups were bilaterally injected with 4-μl AAV9-hsyn-EGFP (3.4×10^{13} gc ml^{-1}; Addgene) or 4-μl AAV9-hsyn-ACh3.0 (1.8×10^{13} gc ml^{-1}) per hemisphere or a combination of 2-μl AAV9-hsyn-EGFP (3.4×10^{13} gc ml^{-1}; Addgene) and AAV9-hsyn-mCherry (3.6×10^{13} gc ml^{-1}; Addgene) per hemisphere. Viruses were injected at 10 nl s^{-1}, and the needle was left in the sinus for 30 s following the injection. Incision sites were sealed with Vetbond glue, and pups were moved to a heating pad. Once the entire litter was injected, pups were gently rubbed with home cage bedding and nesting material and returned to their home cage. Chat-Cre$^{+/0}$Ai162$^{F/0}$ (ref. [67]) mice endogenously expressed GCamp6s in cholinergic neurons and terminals and were not injected with virus. Similarly, Slc17a7-cre/Camk2α-tTA/TITL-GCaMP6f and Thy1-GCaMP6f mice expressed GCaMP6f in cortical excitatory neurons.

Surgical procedures

All surgical implantation procedures were performed on adult mice (>P50). Mice were anesthetized using 1–2% isoflurane and maintained at 37 °C for the duration of the surgery. The skin and fascia above the skull were removed from the nasal bone to the posterior of the intraparietal bone and laterally between the temporal muscles. The surface of the skull was thoroughly cleaned with saline, and the edges of the incision were secured to the skull with Vetbond. A custom titanium headpost was secured to the posterior of the nasal bone with transparent dental cement (Metabond, Parkell), and a thin layer of dental cement was applied to the entire dorsal surface of the skull. Next, a layer of cyanoacrylate (Maxi-Cure, Bob Smith Industries) was used to cover the skull and left to cure approximately 30 min at 22–24C room temperature to provide a smooth surface for transcranial imaging.

For simultaneous ECoG implants, a dental drill was used to make a small craniotomy (-1 mm) lateral to V1 in the right hemisphere. A silver ball electrode was placed in the craniotomy and a silver reference wire implanted in the contralateral cerebellar hemisphere. A ground wire was wrapped around a skull screw placed in the ipsilateral intraparietal bone. For simultaneous basal forebrain stimulation in a subset of animals, stainless steel bipolar stimulating electrodes (125-μm diameter, Invivo1) were implanted at the following coordinates (anterior–posterior (AP) = −0.5 mm, mediolateral (ML) = 1.6 mm, dorsoventral (DV) = 4 mm, angle = 0° or AP = −0.5 mm, ML = 3.3 mm, DV = 3.7 mm, angle = 20°) to target the nucleus basalis in the right hemisphere. Stimulation comprised a brief burst at 100 Hz (1-ms pulse width, 20 pulses, 60–100 μA). Desynchronization in cortical ECoG was used to verify correct electrode placement and to titrate the stimulation intensity.

Widefield imaging

Widefield calcium and cholinergic imaging was performed using a Zeiss Axiozoom with a PlanNeoFluar Z ×1, 0.25 numerical aperture objective with a 56-mm working distance. Epifluorescent excitation was provided by an LED bank (Spectra X Light Engine, Lumencor) using three output wavelengths: 395/25 nm, 470/24 nm and 575/25 nm. Emitted light passed through a dual-camera image splitter (TwinCam, Cairn Research) and then through either a 525/50-nm or 630/75-nm emission filter (Chroma) before it reached two scientific CMOS (sCMOS) cameras (Orca-Flash V3, Hamamatsu). Images were acquired at 512 × 512 resolution after 4× pixel binning, and each channel was acquired at 10 Hz with 20-ms exposure. Images were saved to a solid-state drive using HCImage software version 4.5.1.3 (Hamamatsu).

Backscatter illumination was provided by LEDs (Thorlabs M530L4 and M625L4) centered and narrowly filtered at 530 nm and 625 nm coupled to a 1,000-μm diameter bifurcated fiber (BFY1000LS02) that terminated 45° incident to the brain surface. Image frames capturing backscatter at 530 nm and 625 nm were acquired at 10 Hz and interleaved with the usual fluorescence emission acquisition.

All imaging was performed during the second half of the light cycle in awake, behaving mice that were head-fixed so that they could freely run on a cylindrical wheel[3,4,68]. A magnetic angle sensor (Digikey) attached to the wheel continuously monitored wheel motion. Mice received at least three wheel-training habituation sessions before imaging to ensure consistent running bouts (Extended Data Fig. 4). During widefield imaging sessions, the face (including the pupil and whiskers) was illuminated with an infrared LED bank and imaged with a miniature CMOS camera (Blackfly s-USB3, Flir) with a frame rate of 10 Hz. To monitor the ECoG, we used a DP-311A differential amplifier with active headstage (Warner Instruments). Signals were amplified 1,000×, filtered between 0.1 and 1,000 Hz and digitized at 5,000 Hz using a Power 1401 acquisition board (CED).

Visual stimulation and air puffs

Small (20° diameter) sinusoidal drifting gratings (2 Hz, 0.04 cycles per degree, 100% contrast) were generated using Psychtoolbox in MATLAB and presented on an LCD monitor at a distance of 20 cm. Stimuli were presented for 1–2 s. Air-puff stimuli were delivered using a thin metal tube aimed at the fur along the back and coupled to a solenoid valve (Clark Solutions) that delivered brief (200-ms) puffs of compressed air.

Histology

Histological validation was performed on a subset of animals at the conclusion of imaging experiments. Mice were deeply anesthetized with isoflurane and perfused transcardially with PBS followed by 4% paraformaldehyde in PBS. Brains were postfixed overnight at 4° and embedded in 1% agarose, and 50-μm sagittal sections were cut on a vibratome (VT1000, Leica). Slices were pretreated in blocking solution (2% normal goat serum, 0.1% Triton X-100 in PBS) for 4 h and then incubated with primary antibodies at 1:1,000 (either rabbit anti-GFP and guinea pig anti-NeuN (Invitrogen) or mouse anti-GFP and rabbit anti-GABA (Invitrogen)) at 4° for 24 h. The following day, slices were washed with PBS and incubated in secondary antibodies (either anti-rabbit Alexa Fluor 488 and anti-guinea pig Alexa Fluor 647 (Invitrogen) or anti-mouse Alexa Fluor 488 and anti-rabbit 647 (Invitrogen)) at 1:1,000 for 2 h at room temperature. Slices were washed three times in PBS and then mounted on glass slides in Vectashield antifade mounting medium (Vector Laboratories). Widefield images were acquired on an Olympus BX53 fluorescence microscope. Confocal images were taken with a Zeiss LSM 900.

ACh3.0 imaging ex vivo

Under isoflurane anesthesia, mice were decapitated and coronal slices (~300 μm thick) were cut in ice-cold external solution containing (in mM) 100 choline chloride, 25 $NaHCO_3$, 1.25 NaH_2PO_4, 2.5 KCl, 7 $MgCl_2$, 0.5 $CaCl_2$, 15 glucose, 11.6 sodium ascorbate and 3.1 sodium pyruvate, bubbled with 95% O_2 and 5% CO_2. Slices were transferred to artificial cerebrospinal fluid (ACSF) containing (in mM) 127 NaCl, 25 $NaHCO_3$, 1.25 NaH_2PO_4, 2.5 KCl, 1 $MgCl_2$, 2 $CaCl_2$ and 15 glucose, bubbled with 95% O_2 and 5% CO_2. After an incubation period, slices were moved to a modified recording chamber under the objective of the widefield microscope and constantly perfused with oxygenated ACSF. Slices were imaged using the same protocol as during in vivo imaging sessions (10 Hz, 20-ms exposure). A glass pipette filled with 20 mM carbachol was mounted in a micromanipulator and lowered to just above the slice. A Picospritzer (Parker Hannifin Corp) was used to deliver 200-ms puffs of carbachol. During some trials, scopolamine (20 μM) was added to the ACSF before carbachol puffs were applied.

Pharmacology

Animals were injected with saline, scopolamine hydrobromide (Tocris Bioscience, 0.5 mg kg^{-1} intraperitoneally (i.p.)), or mecamylamine hydrochloride (Tocris Bioscience, 1 mg kg^{-1} i.p.) 15 min before imaging sessions. The order of drug and vehicle injection across sessions was randomized across animals.

Data analysis

All analyses were conducted using custom-written scripts in MATLAB version 2021a (Mathworks).

Statistics and reproducibility. All statistical analyses were conducted using custom-written scripts in MATLAB and Prism 9 (GraphPad). All statistical results are listed in Supplementary Table 2. Exact P values for Figs. 4 and 5 are shown in Supplementary Table 3. Sample sizes were not statistically predetermined but are similar to those reported in previous publications[8,11]. For parametric analyses (ANOVAs and t-tests), normality and equal variances were not formally tested, but individual data points are provided.

Each experiment was conducted in one or two sessions per animal, and analyses were performed on data averaged between sessions, except for stratified permutation tests for correlations where state data were pooled across sessions for each animal. Experiments were not independently replicated. The order of drug and vehicle sessions within each pharmacology group was randomized. Data collection and analyses were not performed blind to the conditions of the experiments. A few animals (one mouse injected with mecamylamine and two injected with scopolamine) were excluded from state-dependent analysis because of insufficient number of sustained facial movement or locomotion states. No animals were excluded from other analyses.

Histology analysis. For cellular quantification, two fields of view in each region were captured per mouse using a ×10 objective (Zeiss). jRCaMP1b-positive cells were identified using the Analyze Particles function in ImageJ version 1.53t. Expression of ACh3.0 or GABA was assessed by first quantifying the density of signal for each cell and comparing to a null distribution from a pixel-shifted control image. Expression was considered positive for cells with signal greater than two standard deviations above control. Statistical comparisons between frontal, somatosensory and visual areas were made using a one-way repeated measures ANOVA.

Preprocessing of imaging data. Images with a size of 512 × 512 pixels were downsampled to 256 × 256 pixels, and frames were grouped by excitation wavelength (395 nm, 470 nm and 575 nm). For dual-color imaging, green and red images were acquired using different cameras and registered via automatic 'rigid' transformation using imregtform

in MATLAB. In some cases, registration points were manually selected, and a 'similarity' geometric transformation was applied. Images were then detrended and baseline corrected to calculate $\Delta F/F$ images. Specifically, for each pixel, a 100th-order fir1 filter with 0.001-Hz frequency cutoff was applied to extract the low-pass-filtered signal. This low-pass signal was used as baseline ($F0$), and $\Delta F/F$ for each pixel was calculated as $(F - F0)/F0$, where F is the raw unfiltered signal. $\Delta F/F$ values were used for all subsequent analyses. Images were registered to the CCFv3 using manually selected control points and similarity-based geometric transformation. Time series for individual brain parcels were then extracted by averaging $\Delta F/F$ values across all pixels within a parcel.

Hemodynamic correction. Common methods for correction of hemodynamic artifacts are typically based on linear regression of a neural activity-dependent signal against an activity-independent signal and performed on a pixel-by-pixel basis, ignoring the spatial correlations among neighboring pixels that exist within and between the two signals. However, accounting for such correlations can be advantageous for mitigating the effects of noise. We experimentally confirmed that excitation of ACh3.0 with 395-nm light results in fluorescence with substantially reduced dependence on ACh (Extended Data Fig. 2), enabling us to use this approach to correct the signal collected with 470-nm excitation. We now present our mathematical formulation for hemodynamic artifact removal as the optimal linear predictor for the neuronal time series, given the 470-nm and 395-nm excitation signals.

Here, y_1 and y_2 are $p \times 1$ random signals corresponding to p pixels of the 470-nm and 395-nm signals, respectively. We use x and z to represent mutually uncorrelated $p \times 1$ random signals corresponding to p pixels of the ACh-dependent and ACh-independent (hemodynamic) signals, respectively. We consider the following linear model:

$$y_1 = x + z + \eta,$$

$$y_2 = Az + \xi,$$

where η and ξ are white Gaussian $p \times 1$ noise signals and A is an unknown $p \times p$ real invertible matrix. Given the above-mentioned model, our goal is to estimate the signal x.

It can be verified that the optimal linear estimator of x in the sense of minimum mean square error is given by the following:

$$\hat{x} = H \begin{pmatrix} y_1 \\ y_2 \end{pmatrix}, H = \Sigma_{xy} \Sigma_y^{-1},$$

where $y = \begin{pmatrix} y_1 \\ y_2 \end{pmatrix}$ is given by stacking y_1 on top of y_2, $\sum_y = \mathbb{E}[yy^T]$ is the autocorrelation matrix of y, and $\sum_{xy} = \mathbb{E}[xy^T]$ is the cross-correlation matrix between x and y. Although Σ_y can be estimated directly from the observations, this is not the case for Σ_{xy}, as it depends on the unknown signal x. Nevertheless, we show that Σ_{xy} can be expressed as follows:

$$\Sigma_{xy} = \left(\sum_{y_1} - \sigma_\eta^2 I - \left(\sum_{y_1 y_2} \left(\sum_{y_2} - \sigma_\xi^2 I \right)^{-1} \sum_{y_2}^{-1} \Sigma_{y_1 y_2}^T \right)^T \quad 0 \right),$$

where σ_η^2 and σ_ξ^2 are the noise variances of η and ξ, respectively, and I is the $p \times p$ identity matrix. Importantly, all quantities in the formula for Σ_{xy} can be estimated directly from the observations of y_1 and y_2. The noise variances σ_η^2 and σ_ξ^2 were evaluated according to the median of the singular values of the corresponding correlation matrices Σ_{y1} and Σ_{y2}.

Proof for the formula for Σ_{xy}:

$$\sum_{xy} = \left(\sum_{xy_1} \quad \Sigma_{xy_2} \right),$$

$$\Sigma_{xy_1} = \Sigma_x,$$

$$\Sigma_{xy_2} = 0,$$

$$\Sigma_{y_1} = \Sigma_x + \Sigma_z + \Sigma_\eta,$$

$$\sum\nolimits_{y_2} = A\Sigma_z A^T + \Sigma_\xi,$$

$$\sum\nolimits_{y_1 y_2} = \Sigma_z A^T.$$

Using these equations, we can extract $\Sigma_z = \left(\sum_{y_1 y_2} (\Sigma_{y_2} - \Sigma_\xi)^{-1} \sum_{y_2}^{-1} \Sigma_{y_1 y_2}^T \right)^T$, which leads to the following:

$$\Sigma_{xy_1} = \Sigma_{y_1} - \Sigma_\eta - \left(\sum_{y_1 y_2} (\Sigma_{y_2} - \Sigma_\xi)^{-1} \sum_{y_1 y_2}^T \Sigma_{y_1 y_2}^T \right)^T.$$

Note that in the case of a single pixel (that is, $p = 1$), our estimator reduces to a simple regression based on pixelwise correlations. However, taking p to be all pixels at once is both computationally expensive and unnecessary. Therefore, we performed these evaluations locally, where the time trace of each pixel was computed based on a patch of its nearest spatial neighbors. The size of the patch was determined according to the amount of time samples available. Using a bigger patch would lead to bigger covariance matrices to be estimated and therefore requires longer time traces. For our sessions a patch size of 9×9 was empirically selected as most adequate.

Validation of hemodynamics correction. The spatial regression approach that we present here was validated by comparing results with other known hemodynamics correction strategies. Several benchmarks were used to determine the effectiveness of our method. First, we and others have observed that strong stimuli, such as a high-contrast visual stimulus, evoke negative dips in fluorescence signals that are driven by hemodynamic photon absorption[40,41]. Here, we compared this visual stimulus-evoked negativity in V1 of GFP-mCherry-expressing mice for uncorrected $\Delta F/F$ signals (measured for 470-nm or 575-nm excitation) and $\Delta F/F$ signals corrected by either spatial or pixelwise regression of signals collected at 395-nm excitation. Visual trials were normalized by subtracting the baseline mean in the −2-s to 0-s prestimulus period, and the minimum normalized $\Delta F/F$ values at 0 s to 5 s after stimulus onset were calculated for each trial. These values were then averaged across all trials in an animal, and statistical comparisons were made within data from each mouse between the three methods using protected paired t-tests following repeated measures ANOVA. A complementary approach involves the measurement of hemodynamic absorption from changes in the reflectance ('backscatter') of green photons while simultaneously performing fluorescence imaging[40,41]. Here, we carried out pixelwise and spatial regression of uncorrected $\Delta F/F$ signals using 530-nm backscatter data and compared results with 395-nm-based correction. We also determined the spatial homogeneity of hemodynamic correction with the different correction methods by examining the averaged visual stimulus-evoked negativity in GFP and mCherry fluorescence across all cortical parcels. Furthermore, we compared the visual stimulus-evoked negativity of ACh3.0 in V1 for uncorrected $\Delta F/F$ signals (measured for 470-nm excitation) and $\Delta F/F$ signals corrected by either spatial or pixelwise regression of signals collected at 395-nm excitation. Finally, we also assessed the efficiency of the different correction approaches to reduce the variance in $\Delta F/F$ signals collected from GFP-expressing control mice, where all fluctuations are assumed to result primarily from hemodynamic variation. Statistical comparisons on $\Delta F/F$ maximum negativity values post air puff were performed in a similar manner as described above for visual stimuli.

Preprocessing of behavior data. Facial movements were extracted from face videography using FaceMap[9]. The toolbox applies singular value decomposition to the face movie to extract the 1,000 dimensions or principal components that explain the distinct movements apparent on the face of the mouse. Here, we included the top 25 principal components for regression analyses and PC1 for other analyses. To extract facial movement states, we focused on periods of quiescence only, because locomotion is consistently associated with increased facial movement. First, PC1 data were Z-score normalized within a session, and the high and low thresholds corresponding to 60% and 40% quantiles in the data distribution during quiescence only, respectively, were extracted for that session. Data were then smoothed using a 1-s window moving-average filter, and epochs during which smoothed data continuously exceeded the high and low Z-thresholds for at least 0.5 s were considered high and low facial movement states, respectively.

Wheel position was determined from the output of the linear angle detector. The circular wheel position variable was first transformed to the [−π, π] interval. The phases were then circularly unwrapped to obtain running distance as a linear variable, and locomotion speed was computed as a differential of distance (cm s^{-1}). A change-point detection algorithm detected locomotion onset and offset times based on changes in standard deviation of speed. First, moving standard deviations of speed were computed in 2-s windows, which was the temporal resolution of the change-point analysis. Initial locomotion onset or offset times were then estimated from periods when the moving standard deviations exceeded or fell below an empirical threshold of 0.005. These estimates were refined by computing the time points corresponding to the maximum of the moving forward–backward Z-score in 2-s windows around each onset and offset time. Locomotion epochs that were too short (<1 s) or for which the average speed was too low (<2 cm s^{-1}) were removed.

Postprocessing analysis

Imaging data from individual parcels were used for subsequent analyses. Some medial Allen Mouse Brain CCFv3 parcels (prelimbic (PL), anterior cingulate area (ACA) and ventral retrosplenial (RSPv)) were masked out because of prominent vasculature along the midline. Colliculus regions (superior colliculus (SC) and inferior colliculus (IC)) were also removed, resulting in a final total of 23 Allen Mouse Brain CCFv3 parcels per hemisphere (Extended Data Fig. 2). The primary visual cortex (V1 or VISp) and the secondary motor area in the frontal cortex (M2 or Mos) were selected as representative areas for some population summaries and statistical comparisons. The anterior–posterior spatial ranking of Allen Mouse Brain CCFv3 areas was determined by calculating the relative centers of mass for each parcel (Extended Data Fig. 2). The ordering was as follows (from anterior to posterior): Mos, Mop, SSp-m, SSp-ul, SSp-n, SSp-ll, SSp-un, SSp-tr, SSp-bfd, SSs, PTLp, VISam, AUD, RSPagl, RSPd, VISal, VISpm, Tea, VISli, VISl, VISp, VISpor and VISpl.

Basal forebrain stimulation-evoked activity. Trials in which basal forebrain stimulation caused locomotion were automatically excluded. Data were normalized by subtracting the baseline mean in the prestimulus period (−2 s to 0 s). Difference $\Delta F/F$ data were averaged across all trials within an animal and summarized as mean ± standard error of mean (s.e.m.) across animals.

Regression with behavioral variables. Linear regression of continuous data from full imaging sessions was used to predict ACh3.0 and jRCaMP1b activity in each parcel using zero-lagged analog behavioral variables as predictors. Tenfold cross validation was performed by partitioning the time series into ten chunks and using independent test partitions in each fold. The prediction accuracy was calculated on testing data in each of the ten folds and averaged to obtain a final cross-validated R^2. The full regression model was built using FaceMap PC1–PC25, pupil area and wheel speed. The model was fit using ridge

regression (ridgeMML.m[8]) in which the regularization penalty was estimated separately for each parcel using marginal maximum likelihood estimation[8]. Reduced models were generated by shuffling specified variables in time. Cross-validated R^2 values from the reduced models were subtracted from those from the full model to obtain ΔR^2 values representing the unique contribution of that variable. In addition, single-variable models were fit to extract individual cross-validated R^2 values for specified behavioral variables. Friedman's ANOVA was used to assess whether full-model cross-validated R^2 values are significantly different across brain areas. Spearman's rank-order correlation was used to assess the relationship between mean cross-validated R^2 values and the anterior–posterior positioning of Allen Mouse Brain CCFv3-defined parcels. Cross-validated R^2 and ΔR^2 values were averaged across parcels in one hemisphere, and comparisons between behavioral variables were performed using a Friedman's ANOVA, followed by post hoc Wilcoxon signed-rank tests.

State transitions and sustained states. Behavioral states were categorized into high and low states (high or low facial movement and quiescence or locomotion) based on movement, as described above (Preprocessing of Behavior Data). Changes at transition from the low to high movement state (facial movement onset or locomotion onset) were defined as state transients (Fig. 3a). For locomotion onset, only locomotion trials that contained at least 5 s of running and were preceded by a minimum 10 s of quiescence were included. For high facial movement state onset, if a high facial movement state was preceded by at least 4 s of a low facial movement state, the transition between the two states was used as the high state onset time point. For each animal, state transients were quantified by first subtracting mean pre-onset (−5 s to −3 s for locomotion and −4 s to −2 s for facial movement) from post-onset $\Delta F/F$ values and averaging data across all state transitions and then calculating the peak $\Delta F/F$ value at 0 s to 1 s after onset. Whole-cortex-averaged transients were obtained by averaging peak $\Delta F/F$ values across all parcels in one hemisphere, and a one-sample Student's t-test was conducted to test significant differences from zero. A two-way repeated measures ANOVA was used to assess any significant differences in state transients across brain areas and behavioral states. Spearman's rank-order correlation was used to assess the relationship between mean peak $\Delta F/F$ values and the anterior–posterior positioning of Allen Mouse Brain CCFv3-defined parcels.

Sustained behavioral states were defined as high or low movement states that persisted for several seconds (Fig. 3a). For sustained locomotion states, it was required that locomotion started at least 3 s before and ended at least 3 s after the state boundaries. Similarly, for sustained quiescence states, it was required that any locomotion did not occur at least 10 s before and 10 s after the quiescent epoch. Sustained high and low facial movement states were extracted during quiescence only. The minimum duration of sustained states was set to 5 s. State data were then compared between low FaceMap, high FaceMap and locomotion states. To ensure accurate comparison between states, the number of state epochs and total duration within each epoch were matched across states within each session. ACh3.0, RCaMP1b and Chat-Gcamp6s $\Delta F/F$ responses during these three states were quantified for each parcel, and whole-cortex-averaged responses were obtained by averaging $\Delta F/F$ values across all parcels in one hemisphere. A two-way repeated measures ANOVA was used to assess whether $\Delta F/F$ responses varied across brain areas and behavioral states, followed by post hoc paired t-tests to test differences between high and low FaceMap states as well as locomotion and high FaceMap state. The response to facial movement and locomotion were quantified as difference between high and low FaceMap $\Delta F/F$ values and between locomotion and high FaceMap $\Delta F/F$ values, respectively. Spearman's rank-order correlation was used to assess the relationship between difference $\Delta F/F$ values and anterior–posterior rank of Allen

Mouse Brain CCFv3-defined parcels. ACh3.0 amplitude during high FaceMap state was compared between frontal-motor areas (averaged $\Delta F/F$ across areas MOp and MOs) and visual areas (averaged $\Delta F/F$ across areas VISp, VISpm, VISam, VISl, VISli, VISpl, VISpor and VISal) with a paired t-test.

For the pharmacology experiments, the effect of drugs on cortical activity related to high facial movement states in frontal-motor or visual areas was computed by taking a difference of $\Delta F/F$ between drug and saline sessions within each animal and performing one-sample t-tests. The spatial difference in drug's effects between visual and motor areas was assessed via paired t-tests on the difference $\Delta F/F$ values between visual and motor areas.

ECoG processing. The multitaper spectrogram in Fig. 1 was estimated from the raw ECoG signal using the Chronux toolbox version 2.12 (using sliding windows of 3 s with 0.5-s overlap). ECoG power was calculated for each behavioral state by estimating the bandpower in high- (30–100 Hz) and low-frequency (1–10 Hz) bands. The ECoG high- and low-frequency power values were compared between high and low FaceMap states and between locomotion and high FaceMap states using Student's paired t-tests.

State-dependent correlations. Time-lagged correlations between every pair of Allen Mouse Brain CCFv3 parcels in ACh3.0 or jRCaMP1b signals were computed by performing cross-correlations with 500-ms time lags and extracting the maximum correlation coefficient. The resulting parcel-wise correlation matrices were calculated during sustained behavioral states with a minimum duration of 5 s to allow enough time frames for lagged correlations. To ensure accurate comparison in correlations between states, the number of state epochs and total duration within each epoch were matched for locomotion and high and low facial movement states within each session. Correlation matrices were calculated for each state epoch, and all epochs and sessions for each animal were averaged to obtain one correlation matrix per animal per state. Cross-correlations between ACh3.0 and jRCaMP1b activity for distinct behavioral states were calculated in a similar manner except that the correlations were performed between the two signals within a parcel. Correlation matrices were compared between locomotion and high facial movement states as well as between high facial movement and low facial movement states. To assess the significance of differences in pairwise correlations between states (high versus low facial movement and locomotion versus high facial movement), a stratified permutation test was used. In each permutation, state labels were shuffled across epochs within the data for each animal, and the corresponding correlation matrices were averaged across all epochs of a particular state to obtain one permuted correlation matrix per state per animal. These values were then averaged across animals to obtain a mean difference between states. This was repeated 10,000 times to build a null distribution of mean differences that was compared against the observed mean difference to determine P values. Multiple-comparisons correction was performed by setting the false discovery rate (FDR) to $q < 0.01$ and using the Benjamini–Yekutieli method in the fdr_bh.m toolbox in MATLAB. Correlation values and adjusted P values are available in Supplementary Table 3.

Reporting summary
Further information on research design is available in the Nature Portfolio Reporting Summary linked to this article.

Data availability
The full datasets generated and analyzed in this study are available from the corresponding authors on reasonable request. Source data for figures have been made available as Excel files. Source data are provided with this paper.

Code availability

Custom-written MATLAB scripts used in this study are available at https://github.com/cardin-higley-lab/Lohani_Moberly_et_al_2022. Source data are provided with this paper.

References

67. Larsen, R.S. et al. Activation of neuromodulatory axon projections in primary visual cortex during periods of locomotion and pupil dilation. Preprint at *bioRxiv* https://doi.org/10.1101/502013 (2018).
68. Batista-Brito, R. et al. Developmental dysfunction of VIP interneurons impairs cortical circuits. *Neuron* **95**, 884–895.e9 (2017).

Author contributions

S.L., A.H.M., M.J., Y.L., M.J.H. and J.A.C. designed the experiments. S.L. and A.H.M. collected the data. S.L., A.H.M., H.B. and B.L. analyzed the data. S.L., A.H.M., M.J.H. and J.A.C. wrote the manuscript.

Competing interests

The authors declare no competing interests.

Additional information

Extended data is available for this paper at https://doi.org/10.1038/s41593-022-01202-6.

Supplementary information The online version contains supplementary material available at https://doi.org/10.1038/s41593-022-01202-6.

Correspondence and requests for materials should be addressed to Michael J. Higley or Jessica A. Cardin.

Peer review information *Nature Neuroscience* thanks the anonymous reviewers for their contribution to the peer review of this work.

**Reprints and permissions information** is available at www.nature.com/reprints.
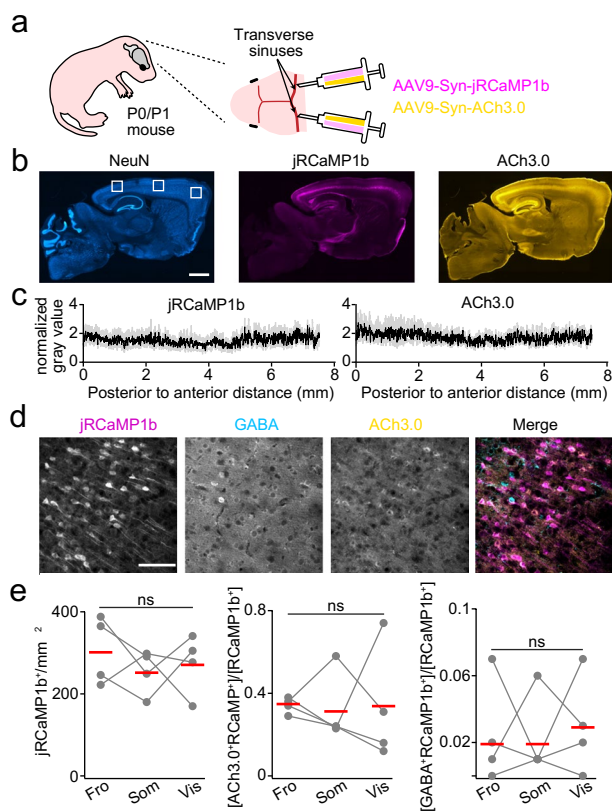
Extended Data Fig. 1 | Viral expression of the cholinergic reporter ACh3.0 and the calcium indicator jRCaMP1b. a, Schematic of the neonatal sinus injection approach. **b**, Example sagittal widefield fluorescent images from an adult mouse expressing jRCaMP1b (magenta) and ACh3.0 (yellow). Sections were immunostained for the neuronal marker NeuN (blue). Scale bar; 1 mm. **c**, Average intensity (mean ± SEM, n = 4 mice) from posterior to anterior neocortex normalized to NeuN intensity values for jRCaMP1b (left) and ACh3.0 (right). **d**, Example confocal images from an adult mouse co-expressing jRCaMP1b and ACh3.0. Sections were immunostained for GABA (cyan) to label inhibitory cells.

Scale bar: 100 µm. **e**, Average cell counts (n = 4 mice) from fields of view from frontal (Fro), somatosensory (Som), or visual (Vis) cortex (example insets marked by boxes in (**b**). For each field of view, data indicate the number of positive cells per mm^2 for jRCaMP1b (left, $F_{(2,6)} = 0.455$, $p = 0.655$, repeated measures ANOVA), the proportion of jRCaMP1b-positive cells co-expressing ACh3.0 (middle, $F_{(2,6)} = 0.014$, $p = 0.986$, repeated measures ANOVA), and the proportion of jRCaMP1b-positive cells co-expressing GABA (right, $F_{(2,6)} = 0.085$, $p = 0.920$, repeated measures ANOVA).
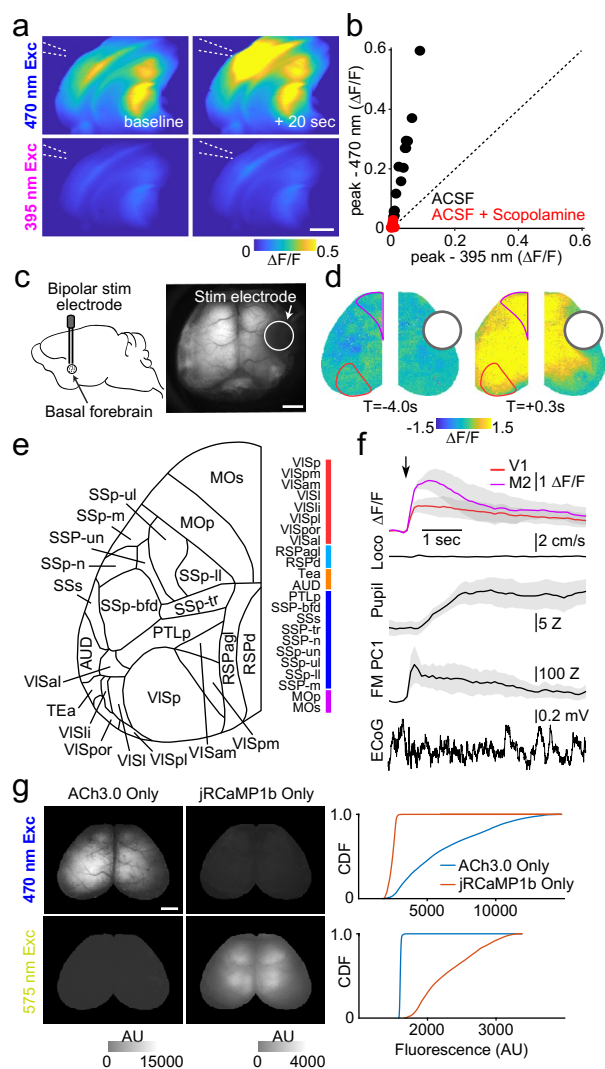
Extended Data Fig. 2 | *Ex vivo* and *in vivo* validation of mesoscopic ACh3.0 signals. a, Example brain slice from an ACh3.0-expressing mouse imaged with 470 nm (blue) and 395 (violet) excitation light on interleaved frames. Images show fluorescence at baseline (left) and 20 s after carbachol (20 μM) was puffed onto the slice (right). Scale bar; 1 mm. **b**, Peak carbachol-evoked ΔF/F responses for 395 nm versus 470 nm excitation, in control ACSF or in the presence of scopolamine (10 μM). **c**, Schematic showing bipolar stimulation electrodes implanted in the basal forebrain (left) and corresponding mesoscopic image showing baseline fluorescence (right). Scale bar; 1 mm. **d**, Example pixel-wise spatial maps of ΔF/F ACh3.0 signal averaged across trials before (left) and after (right) electrical stimulation of the basal forebrain. **e**, Schematic illustrating Allen CCFv3 parcels, corresponding abbreviations and color codes used in main figures. **f**, Mean ± SEM (n = 3 mice) ACh3.0 signal activity evoked by basal forebrain electrical stimulation for V1 (red) and M2 (purple) Allen CCFv3 parcels indicated in e. Corresponding mean ± SEM changes in locomotion, pupil, facial movement (FaceMap PC1) and an example ECoG trace from a single stimulation are illustrated below. **g**, Example images showing fluorescence under 470 nm excitation light (top) and 575 nm excitation light (bottom) in an ACh3.0-expressing mouse (left) and a jRCaMP1b-expressing mouse (right). Scale bar: 1 mm. Cumulative distribution plots of the pixel intensities from the example frames under both illumination conditions are shown on the far right.
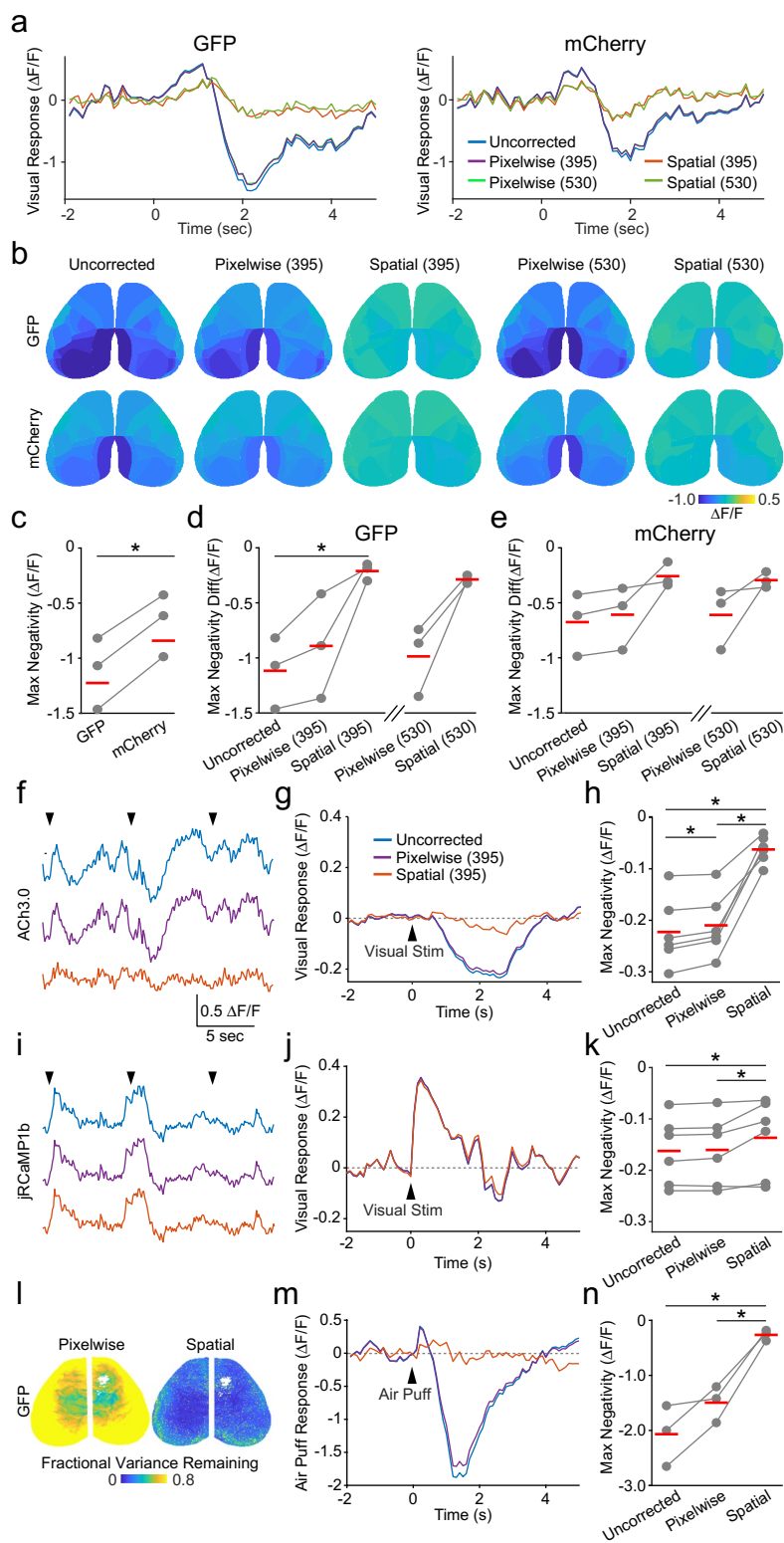
Extended Data Fig. 3 | See next page for caption.

Extended Data Fig. 3 | Spatial regression for correction of hemodynamic artifacts in mesoscopic data. a, GFP/mCherry fluorescence signals measured in V1 during presentation of drifting grating stimuli, illustrating different hemodynamic correction methods. Plots show averaged ΔF/F GFP (left) and mCherry (right) activity evoked by visual stimulation in one example session from a mouse co-expressing GFP and mCherry. Traces are for uncorrected fluorescence (blue) and images corrected using pixel-wise regression of 395 nm fluorescence data (purple) or 530 nm back-scatter data (light green), or spatial regression of 395 nm (orange) or 530 nm (dark green) data. **b**, ΔF/F GFP and mCherry activity across all parcels, evoked by visual stimulation. Population averaged (n = 3 mice) images are from uncorrected data and data corrected using different regression methods. **c**, Individual and population averaged (n = 3 mice) GFP and mCherry values in V1 for visually-evoked ΔF/F negativity (hemodynamic artifact), from uncorrected data. * indicates p < 0.05, two-tailed paired t-test (t(2) = −17.353, p = 0.003). **d**, Individual animal and population mean (n = 3 mice) values for visually-evoked ΔF/F GFP negativity for the different correction methods. * indicates p < 0.05, post hoc two-tailed paired t-tests following repeated measures ANOVA comparing uncorrected, pixelwise (395) and spatial (395) regression methods (F(2,4) =14.754, p = 0.014; uncorrected vs pixelwise: t(2) = −2.499, p = 0.130; uncorrected vs spatial: t(2) = −5.905, p = 0.028; pixelwise vs spatial: t(2) = −2.807, p = 0.107). **e**, as in d for mCherry data (F(2,4) = 6.270, p = 0.059). **f**, ACh3.0 signals measured in V1 during visual stimulus presentation (arrows), illustrating different hemodynamic correction methods. **g**, Average ΔF/F ACh3.0 activity evoked by visual stimulation in one example session with each correction method. **h**, Individual animal and population mean (n = 6 mice) values for visually-evoked ΔF/F negativity with each correction method. * indicates p < 0.05, post hoc two-tailed paired t-tests following repeated measures ANOVA (F(2,10) = 54.423, p < 0.001; uncorrected vs pixelwise: t(5) = −4.758, p = 0.005; uncorrected vs spatial: t(5) = -7.259, p = 0.001; pixelwise vs spatial: t(5) = −7.568, p = 0.001). **i-k**, as in (f-h) for jRCaMP1b data (n = 6 mice) in V1 (F(2,10) = 6.776, p = 0.014; uncorrected vs pixelwise: t(5) = −1.719, p = 0.146; uncorrected vs spatial: t(5) = −2.607, p = 0.048; pixelwise vs spatial: t(5) = −2.610, p = 0.048). **l**, Pixel-wise variance remaining from imaging of a GFP-expressing mouse following hemodynamic correction with pixel-wise (left) or spatial (right) regression of 395 nm fluorescence data. **m**, Average GFP fluorescence in V1 evoked by air-puff stimulus to the animal's flank. Traces are for uncorrected fluorescence (blue) and images corrected using pixelwise (purple) or spatial (red) regression of 395 nm data. **n**, Individual animal and population mean (n = 3 mice) values for air-puff-evoked ΔF/F negativity for the different regression methods. * indicates p < 0.05, post hoc two-tailed paired t-tests following repeated measures ANOVA (F(2,4) = 36.002, p = 0.003; uncorrected vs pixelwise: t(2) = −2.583, p = 0.123; uncorrected vs spatial: t(2) = −6.821, p = 0.021; pixelwise vs spatial: t(2) = −8.203, p = 0.015).
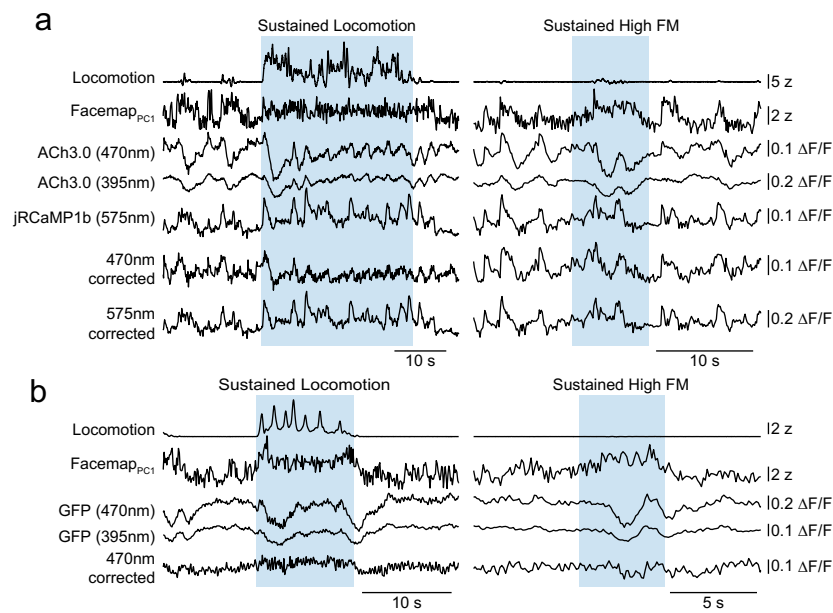
Extended Data Fig. 4 | Examples of hemodynamic correction. a, Example behavioral and neural data time series from a period of sustained locomotion (left) and sustained high facial motion activity (right) in a mouse co-expressing ACh3.0 and jRCaMP1b. Neural data are V1 traces from ACh3.0 under 470 nm and 395 nm excitation light and jRCaMP1b under 575 nm excitation light before and after hemodynamic correction using spatial regression of the 395 nm fluorescence. Correction substantially reduces large negative deflections especially in the ACh3.0 signal. **b**, Same as in (b) for an example GFP-expressing mouse.
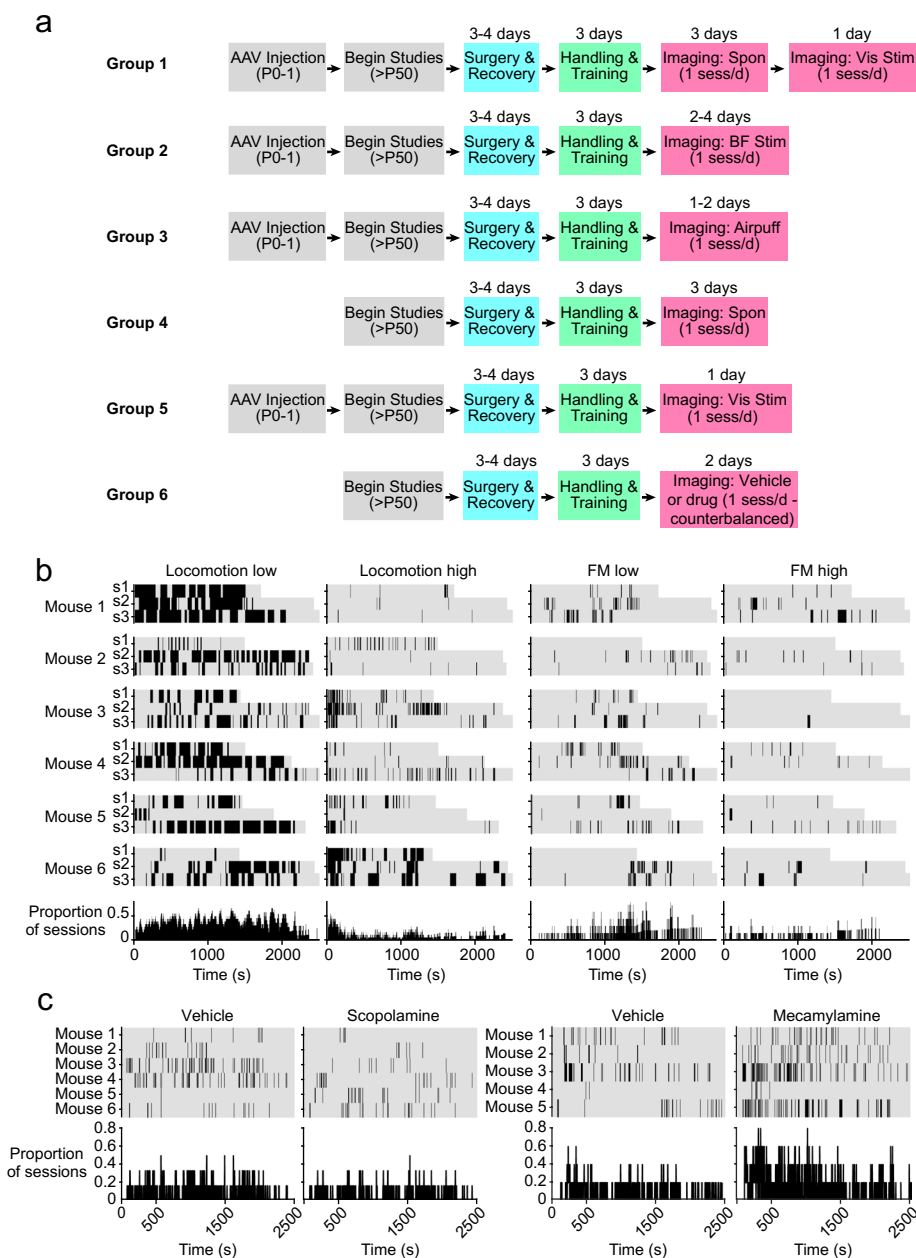
Extended Data Fig. 5 | Experimental timeline and distribution of behavioral states. a, Experimental timeline and group schematic for animals used in the study. **b**, Behavioral raster plots indicating periods of sustained low and high locomotion and sustained low and high facial motion activity across all imaging session in the six dual ACh3.0/jRCaMP1b mice comprising Group 1. Below are histograms indicating the distribution of the sustained states over time. **c**, Behavioral raster plots indicating periods of sustained high face states during imaging sessions in mice comprising Group 6 (scopolamine and mecamylamine injected mice). Below are histograms indicating the distribution of the sustained state over time across the imaging sessions.
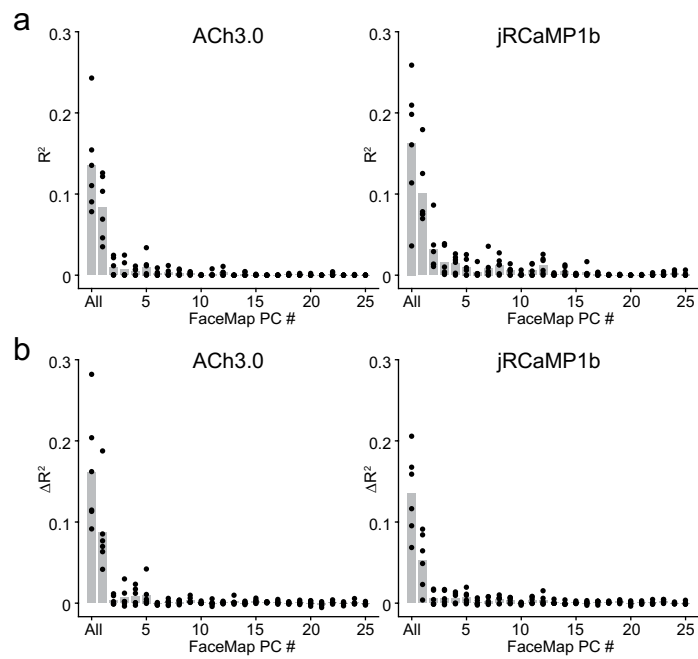
Extended Data Fig. 6 | Relationship between FaceMap principal components and cholinergic and neural activity. a, Cross validated R^2 values (averaged across all parcels in single hemisphere) of ACh3.0 (left) and jRCaMP1b (right) based on regression model including FaceMap principal components 1–25 and each of these FaceMap PCs individually (n = 6 mice). **b**, Unique contribution to the full model (ΔR^2) of FaceMap components 1–25 and each FaceMap component individually (n = 6 mice).
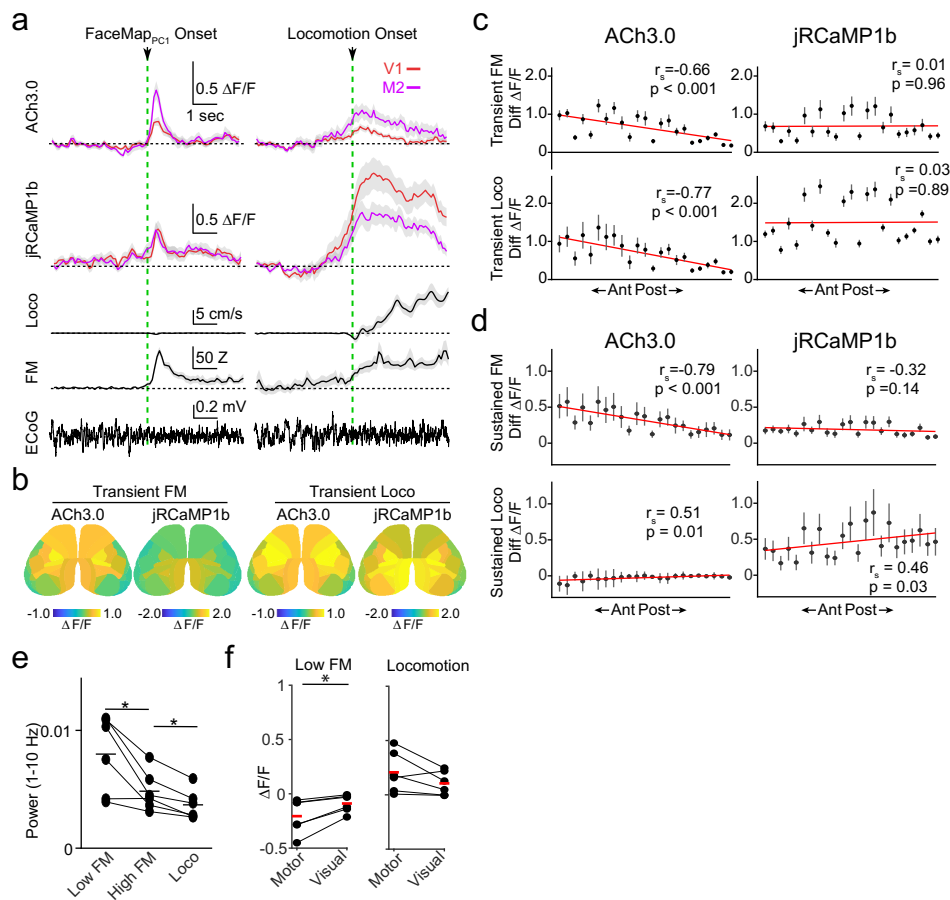
Extended Data Fig. 7 | Spatial heterogeneity in cholinergic and calcium signaling during movement-defined transient and sustained behavioral states. a, Traces show trial-averaged activity (mean ± SEM) for V1 (red) and M2 (purple) aligned to FaceMap PC1 (left) and locomotion (right) transition points for one session, with simultaneous locomotion, pupil area, facial movement (FaceMap PC1) and an example raw ECoG trace shown below. **b**, Average spatial maps (n = 6) showing parcel-wise differences in ACh3.0 and jRCaMP1b activity upon transition to high facial motion (top) and locomotion (bottom), showing peak ΔF/F values at 0 to 1 s post high facial motion or locomotion onset. **c**, Peak (at 0 to 1 s from state transition) ΔF/F difference values (post/pre-onset, mean ± SEM, n = 6 mice) from parcels in the left hemisphere are plotted against their anterior-to-posterior position based on center of mass. r_s indicates Spearman's rank-order correlation coefficient for correlation between mean value and anterior–posterior rank across parcels (FaceMap onset: Ach3.0 r_s = −0.660, p < 0.001; jRCaMP1b r_s = 0.010, p = 0.962; locomotion onset: Ach3.0

r_s = −0.768, p < 0.001; jRCaMP1b r_s = 0.029, p = 0.895). Line indicates linear fit for visualization. **d**, Same as in (c) for ΔF/F difference values (mean ± SEM, n = 6 mice) for sustained states (high-low facial motion PC1 onset, top and locomotion-high facial motion, bottom) parcels (FaceMap: Ach3.0 r_s = −0.789, p < 0.001; jRCaMP1b r_s = 0.321, p = 0.136; Locomotion: Ach3.0 r_s = 0.509, p = 0.013; jRCaMP1b r_s = 0.463, p = 0.026). **e**, Individual animal values and population means for low-frequency (1–10 Hz) ECoG power (n = 6 mice) for sustained low facial motion, high facial motion and locomotion states. *indicates p < 0.05 for post hoc two-tailed paired t-test comparisons (low vs high FM: t(5) = 3.291, p = 0.022; locomotion vs high FM: t(5) = 4.999, p = 0.004) following a significant main effect of behavioral state in repeated measures ANOVA (F(2,10) = 15.459, p = 0.001). **f**, Comparison of Ach 3.0 amplitude (n = 6 mice) in visual and motor areas compared to visual areas during low facial motion and locomotion. *indicates p < 0.05, two-tailed paired t-tests (low FM: t(5) = 3.674, p = 0.014; locomotion t(5) = −1.973, p = 0.106).
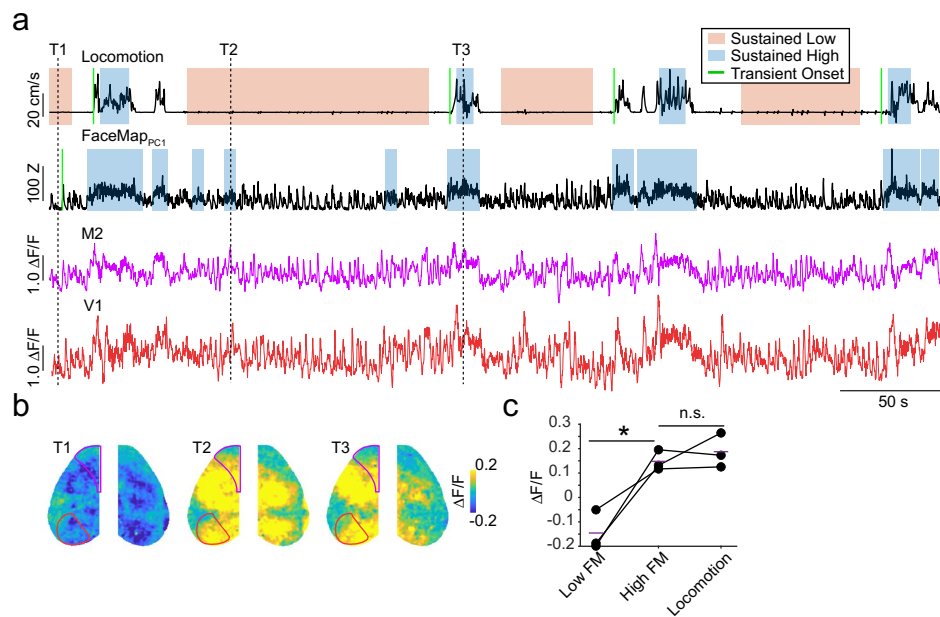
Extended Data Fig. 8 | Cholinergic signal in ChAT-GCaMP mice during movement-defined behavioral states. a, Example time series showing behavioral measures (locomotion and FaceMap PC1) and GCaMP6 signals from the M2 (purple) and V1 (red) parcels in a Chat-Cre$^{+/0}$Ai162$^{F/0}$ mouse. **b**, Representative image frames from a period of no locomotion and low facial motion activity (T1), no locomotion and high facial motion activity (T1) and locomotion and high facial motion activity (T3). **c**, Individual animal values and population mean whole cortex ΔF/F values during sustained low facial motion, high facial motion and locomotion states. Inset shows individual and population mean ΔF/F difference values (n = 3 mice) between high-low facial motion and locomotion-high facial motion. *indicates p < 0.05 for post hoc two-tailed paired t-test comparisons (low vs high FM: t(2) = −4.397, p = 0.048; locomotion vs high FM: t(2) = −0.835, p = 0.492) following repeated measures ANOVA (F(2,4) = 14.798, p = 0.014).
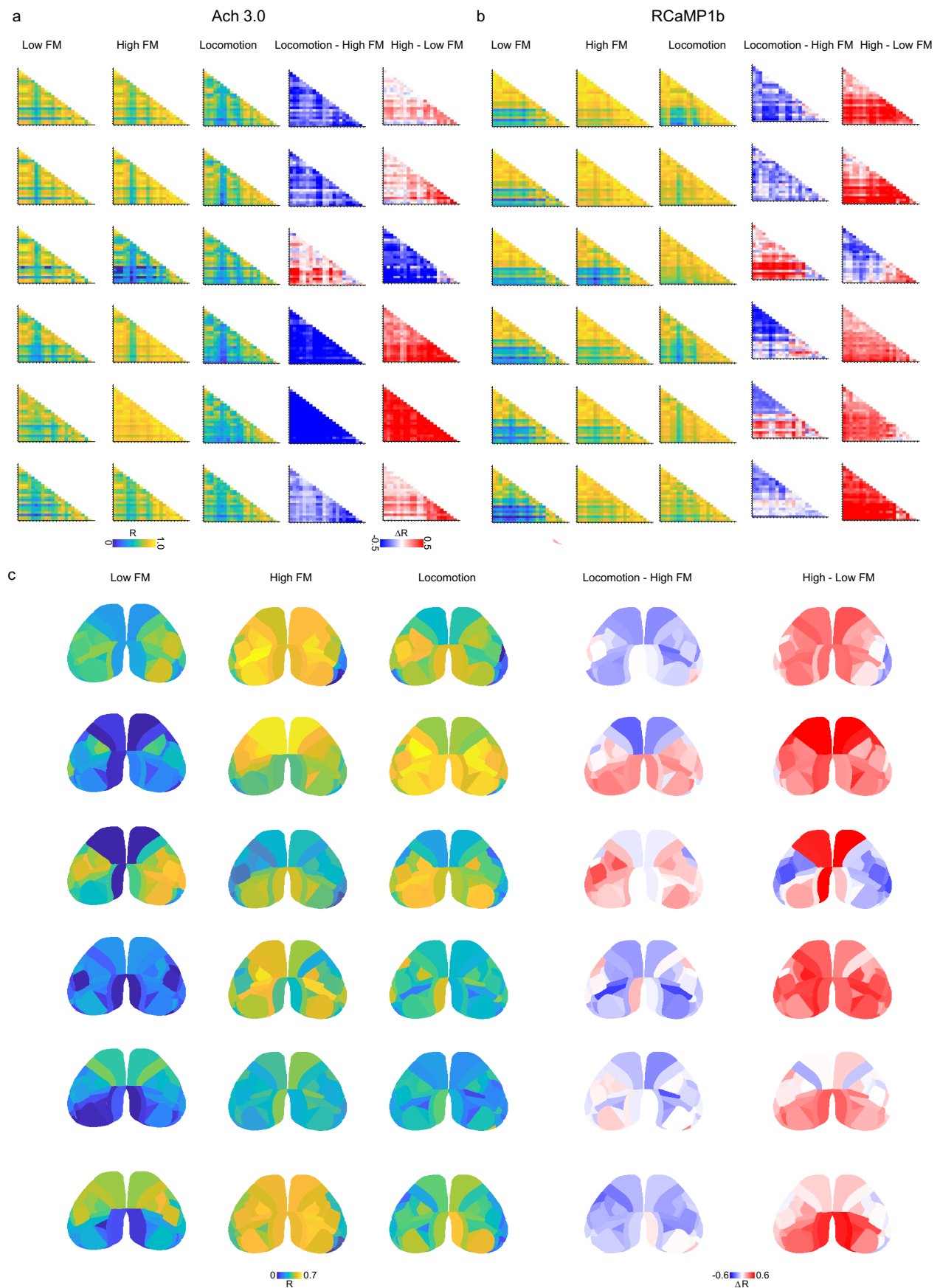
Extended Data Fig. 9 | Correlation matrices for individual animals. a, b, Individual correlation matrices for ACh 3.0 (a) and jrCaMP1b (b) during sustained behavioral states. Each row corresponds to one animal. **c**, Individual brain maps showing correlation between Ach 3.0 and jrCaMP1b during sustained behavioral states. Each row corresponds to one animal.

nature research

Corresponding author(s): Jessica A. Cardin, Michael J. Higley

Last updated by author(s): 9/26/2022

Reporting Summary

Nature Research wishes to improve the reproducibility of the work that we publish. This form provides structure for consistency and transparency in reporting. For further information on Nature Research policies, see our Editorial Policies and the Editorial Policy Checklist.

Statistics

For all statistical analyses, confirm that the following items are present in the figure legend, table legend, main text, or Methods section.

n/a	Confirmed	
☐	☒	The exact sample size (*n*) for each experimental group/condition, given as a discrete number and unit of measurement
☐	☒	A statement on whether measurements were taken from distinct samples or whether the same sample was measured repeatedly
☐	☒	The statistical test(s) used AND whether they are one- or two-sided *Only common tests should be described solely by name; describe more complex techniques in the Methods section.*
☐	☒	A description of all covariates tested
☐	☒	A description of any assumptions or corrections, such as tests of normality and adjustment for multiple comparisons
☐	☒	A full description of the statistical parameters including central tendency (e.g. means) or other basic estimates (e.g. regression coefficient) AND variation (e.g. standard deviation) or associated estimates of uncertainty (e.g. confidence intervals)
☐	☒	For null hypothesis testing, the test statistic (e.g. *F*, *t*, *r*) with confidence intervals, effect sizes, degrees of freedom and *P* value noted *Give P values as exact values whenever suitable.*
☒	☐	For Bayesian analysis, information on the choice of priors and Markov chain Monte Carlo settings
☐	☒	For hierarchical and complex designs, identification of the appropriate level for tests and full reporting of outcomes
☐	☒	Estimates of effect sizes (e.g. Cohen's *d*, Pearson's *r*), indicating how they were calculated

Our web collection on statistics for biologists contains articles on many of the points above.

Software and code

Policy information about availability of computer code

Data collection	All data was collected using commercial software from HCImage (v4.5.1.3 Hamamatsu), Spinview (v1.25.0.52 Flir) and Spike 2 (v9.02 Cambridge Electronic Design)
Data analysis	Data was analyzed using MATLAB (v2019b, Mathworks) and GraphPad Prism (v9.0.1 Graphpad Software). All code is available at https://github.com/cardin-higley-lab/Lohani_Moberly_et_al_2022.

For manuscripts utilizing custom algorithms or software that are central to the research but not yet described in published literature, software must be made available to editors and reviewers. We strongly encourage code deposition in a community repository (e.g. GitHub). See the Nature Research guidelines for submitting code & software for further information.

Data

Policy information about availability of data

All manuscripts must include a data availability statement. This statement should provide the following information, where applicable:
- Accession codes, unique identifiers, or web links for publicly available datasets
- A list of figures that have associated raw data
- A description of any restrictions on data availability

The full datasets generated and analyzed in this study are available from the corresponding authors on reasonable request. The values used to generate correlation matrices between parcel pairs (Figure 4) and correlations between signals within a parcel (Figure 5) have been made available as a supplementary file.

Field-specific reporting

Please select the one below that is the best fit for your research. If you are not sure, read the appropriate sections before making your selection.

☒ Life sciences   ☐ Behavioural & social sciences   ☐ Ecological, evolutionary & environmental sciences

For a reference copy of the document with all sections, see nature.com/documents/nr-reporting-summary-flat.pdf

Life sciences study design

All studies must disclose on these points even when the disclosure is negative.

Sample size	Sample size was chosen as standard in field and is similar to previously published studies (Musall et al., 2019, Allen et al., 2017; Tang and Higley 2020).
Data exclusions	A few animals (one mouse injected with mecamylamine and two injected with scopolamine) were excluded from state-dependent analysis because of insufficient number of sustained face or locomotion states. No animals were excluded from other analyses.
Replication	Most analysis was based on within-animal comparisons. All data points are from independent experiments. In cases where multiple samples were taken from individual animals, statistics (stratified permutation tests with correction) were performed to account for the nested hierarchical experimental design. Cohort replication was not performed.
Randomization	Most data in the study were observational. For pharmacology experiments, the order of vehicle/drug sessions was randomly varied.
Blinding	Most data in the study were observational data from wild-type mice and did not require blinding.

Reporting for specific materials, systems and methods

We require information from authors about some types of materials, experimental systems and methods used in many studies. Here, indicate whether each material, system or method listed is relevant to your study. If you are not sure if a list item applies to your research, read the appropriate section before selecting a response.

Materials & experimental systems

n/a	Involved in the study
☐	☒ Antibodies
☒	☐ Eukaryotic cell lines
☒	☐ Palaeontology and archaeology
☐	☒ Animals and other organisms
☒	☐ Human research participants
☒	☐ Clinical data
☒	☐ Dual use research of concern

Methods

n/a	Involved in the study
☒	☐ ChIP-seq
☒	☐ Flow cytometry
☒	☐ MRI-based neuroimaging

Antibodies

Antibodies used	Rabbit anti-GFP, guinea pig anti-NeuN, mouse anti-GFP, rabbit anti-GABA, anti-rabbit-Alexa Fluor 488, anti-guinea pig-Alexa Fluor 647, anti-mouse-Alexa Fluor 488, anti-rabbit 647 (Invitrogen).
Validation	*Describe the validation of each primary antibody for the species and application, noting any validation statements on the manufacturer's website, relevant citations, antibody profiles in online databases, or data provided in the manuscript.*

Animals and other organisms

Policy information about studies involving animals; ARRIVE guidelines recommended for reporting animal research

Laboratory animals	Adult male and female c57Bl/6 and Chat-Cre mice 2-6 months old.
Wild animals	Did not involve wild animals.
Field-collected samples	Did not involve field-collected samples.
Ethics oversight	Ethical oversight provided by Yale IACUC.

Note that full information on the approval of the study protocol must also be provided in the manuscript.